공학박사 학위논문

# 고분자 전해질막 연료전지 가스확산층의 이방성에 따른 성능 및 열화특성에 관한 연구

**Studies on the performance and degradation characteristics by GDL anisotropy of PEMFC**

2013년 8월


서울대학교 대학원

기계항공공학부

서 정 훈

# 고분자 전해질막 연료전지 가스확산층의 이방성에 따른 성능 및 열화특성에 관한 연구

**Studies on the performance and degradation characteristics by GDL anisotropy of PEMFC**

지도교수 김 민 수

이 논문을 공학박사 학위논문으로 제출함

2013년 4월

서울대학교 대학원
기계항공공학부
서 정 훈

서정훈의 공학박사 학위논문을 인준함
2013년 6월

위 원 장 _____ (인)

부위원장 _____ (인)

위 원 _____ (인)

위 원 _____ (인)

위 원 _____ (인)

# Studies on the performance and degradation characteristics by gas diffusion layers anisotropy of polymer electrolyte membrane fuel cells

A DISSERTATION SUBMITTED TO THE DEPARTMENT OF MECHANICAL AND AEROSPACE ENGINEERING OF SEOUL NATIONAL UNIVERSITY IN PARTIAL FULFILLMENT OF THE REQUIREMENTS FOR THE DEGREE OF DOCTOR OF PHILOSOPHY

By

Jeong Hoon Seo

August 2013

# Abstract

## Studies on the performance and degradation characteristics by gas diffusion layers anisotropy of polymer electrolyte membrane fuel cells

Jeong Hoon Seo
Department of Mechanical and Aerospace Engineering
The Graduate School
Seoul National University

Gas diffusion layers (GDLs) play important roles that include reactant gas transportation, electron conduction, liquid water management and structural supporting of membrane electrode assembly (MEA) in polymer electrolyte membrane fuel cells (PEMFCs). The macro-porous layer has anisotropic characteristics by preferential direction of mechanical properties. The in-plane anisotropy of GDL has both fiber directions that is perpendicular (designated by 90° GDL) and parallel (designated by 0° GDL) to the major flow when fuel cell components are assembled. Deformation and intrusion into the cell channel of GDL are inevitable during the cell assembly. Mechanical bending stiffness direction by the in-plane anisotropy can

influence on the GDL deformation/intrusion and accordingly, the cell performance and durability. For analyzing clearly the effects of the GDL in-plane anisotropy, experimental and numerical studies are conducted.

Firstly, the effects of GDL in-plane anisotropy on cell performance were investigated experimentally. For analyzing correlation between anisotropic bending stiffness of a GDL and geometries of bipolar plates, 6 bipolar plates having 3 different channel/land width ratios and 3 different channel depths are prepared. I-V performance of the fuel cells with 90° GDL are generally higher than those with 90° GDL. On the contrary, high-frequency resistance (HFR) of the fuel cells with 90° GDL is lower than those with 0° GDL due to the higher resistance to force of bipolar plates during fuel cell assembly. In experimental results by different channel/land width ratios, the differences of I-V performances and HFR values between 90° and 0° GDL cells gradually decrease with increasing land/channel width ratio. It is because that anisotropic stiffness effect of the GDLs with wider land is reduced due to the better support. Therefore, less deformation and intrusion into channel of fuel cells with 90° GDL can improve the fuel cell performance. Air pressure drop of all the fuel cells with 90° GDLs was similar to those with 0° GDLs because air flow in channel at sufficient wide channel height of 0.6 mm. The cross-sectional images of GDLs upon compression pressure support the results by 90° GDLs have less deformation. In experimental results by different channel

depths, the differences of air pressure drop values between the 90° and 0° GDL cells were appeared. In shallowest channel, the air pressure drop values of the 0° GDL cells were clearly higher than those of the 90° GDL cells due to more intrusion of 0° GDL into the channel. However, other channels except the shallowest channel appear no significant difference presumably due to the exceptional increase in the air pressure may cause more deformation and poor contact status of the GDLs in the fuel cell.

In dead-end mode, the peak voltage of the 0° GDL cell was also higher than 90° GDL indicating the higher contact resistance in 0° GDL cell. Also, the purge interval of the fuel cell with 0° GDL was also longer than that of the fuel cell with 90° GDL implying the difference of GDL porosity reduction between both to 90° and 0° GDL cells at same cell assembly pressure. The averaged voltages of 90° GDL cell were higher than those of 0° GDL cell and the difference is more obvious at higher current density owing to the higher contact resistance in the higher current density.

Numerical model using commercial computational fluid dynamics (CFD) was conducted for analyzing the effect of anisotropic GDLs on cell performance by gas permeation through the cell channel. Permeability of anisotropic GDLs for applying to model simulation was measured. Afterwards, same geometry as single cell used in chapter 3 was applied in this model. The voltage difference in high current density over 0.9 $A/cm^2$ was relatively distinct, whereas the voltage difference in low current density below 0.9 $A/cm^2$ was negligible. The simulation results show that the higher performance was induced by gas permeation through the cell channels. By the result, it is identified that not only contact resistance by GDL deformation but also gas permeation through the cell channel influence on the cell performance.

Lastly, the effect of in-plane anisotropic characteristics on the mechanical degradation of an MEA was investigated using an AST. The wet/dry cycling method was adopted to cause mechanical degradation of the MEA. I–V performances and HFRs of the 90° GDL cell and 0° GDL cell were measured every 500 cycles and hydrogen crossover rates were measured every 1000 cycles. I–V performance and HRF drop of the 0° GDL fuel cell according to wet/dry cycles was higher because the 0° GDL had lower resistance to stress by repetitive membrane swelling/shrinkage than the 90°

GDL. The increase in the hydrogen crossover rate of the 0° GDL fuel cell was higher than that of the 90° GDL fuel cell because of mechanical degradation of the MEA. Through SEM, it was shown that the MEA deformation of 0° GDL fuel cells was more severe than that of the 90° GDL fuel cell after wet/dry cycles. No spatial gap due to deformation of the 90° GDL under compression was detected; however, a gap for the 0° GDL was observed. These results support our assumptions that a higher resistance of the GDL to repetitive membrane swelling/shrinkage by wet/dry cycles increases the performance and durability of the fuel cell.

It was identified that cell performance can be improved by simple adjustment of GDL arrangement during cell assembly. The results about the effects by geometry of bipolar plates can be helpful for optimum designs of fuel cell components. Also, this effort to minimize the GDL deformation and degradation will bring forward the commercialization of PEMFC.

**Keywords: Polymer electrolyte membrane fuel cell, Gas diffusion layer, GDL anisotropy, degradation, High frequency resistance, wet/dry cycle**

***Identification Number*: 2010-30789**

# Contents

# List of Figures

# List of Tables

# Nomenclature

| | |
|---|---|
| $a_k$ | Activity of water in stream k |
| $A_{cv}$ | Specific surface area of the control volume [$m^{-1}$] |
| $Area_{cv}$ | Surface area of the control volume [$m^2$] |
| $C_{wk}$ | Water vapor concentration at $k^{th}$ interface of the membrane [mol $m^{-3}$] |
| $C_{wlk}$ | Liquid water concentration at $k^{th}$ interface of the membrane [mol $m^{-3}$] |
| $D_{H2,l}$ | Diffusion coefficient of $H_2$ in a liquid water film, [$6.3 \times 10^{-9}$ $m^2$ $s^{-1}$] |
| $D_{O2,l}$ | Diffusion coefficient of $O_2$ in a liquid water film, [$2.4 \times 10^{-9}$ $m^2$ $s^{-1}$] |
| $D_{n,j}$ | Binary diffusion coefficient of species n in gas mixture *j* [$m^2$ $s^{-1}$] |
| $D_w$ | Diffusion coefficient of water [$m^2$ $s^{-1}$] |
| $D_{ø}$ | Effective conductivity (S/m) of GDLs and bipolar plate |
| $F$ | Faraday constant [96487 C mole-of-electrons$^{-1}$] |
| $H_{H2,l}$ | Henry's constant for hydrogen in a liquid water film [$8.9 \times 10^{-9}$ Pa] |
| $H_{O2,l}$ | Henry's constant for oxygen in a liquid water film [$2.12 \times 10^{-9}$ Pa] |
| $h_{rxn}$ | Enthalpy of water formation [kJ $kmol^{-1}$] |
| $h_{fg}$ | Enthalpy of water vaporization [kJ $kmol^{-1}$] |
| $I$ | Local current density [A $m^{-2}$] |
| $I_{o,K}$ | Exchange current density for reaction K [A $m^{-2}$] |
| $m_{n,k}$ | Mass fraction of species n in stream k |
| $M_{m,dry}$ | Equivalent weight of species n [kg $mol^{-1}$] |
| $mass_n$ | Mass of species n [kg] |
| $m_{w,l}$ | Mass fraction of liquid water [kg] |
| $n_d$ | Electro-osmotic drag sufficient |
| $p^{sat}{}_{w,k}$ | Vapor pressure of water in stream k [Pa] |
| $P$ | Pressure [Pa] |

| | |
|---|---|
| $P_n$ | Partial pressure of species n [Pa] |
| $Q$ | Volumetric flow rate [$m^3s^{-1}$] |
| $R$ | Universal gas constant [8.314 J mol-1 $K^{-1}$] |
| $r$ | Condensation rate [$s^{-1}$] |
| $S$ | Source term |
| $S_{he}$ | Heat source term from electrochemical losses for energy equations |
| $S_{hp}$ | Heat source term from water phase change for energy equations |
| $S_{ø}$ | Source term of phase potential [A $m^{-3}$] |
| $t_m$ | Membrane thickness [m] |
| $t_{f,a}$ | Liquid water film on the anode [m] |
| $t_{f,c}$ | Liquid water film on the cathode [m] |
| $T$ | Temperature [K] |
| $u,v,w$ | Velocity in the x, y and z direction, respectively [m $s^{-1}$] |
| $V_{oc}$ | Cell open-circuit voltage [V] |
| $V_{cell}$ | Cell voltage [V] |
| $X_{i,k}$ | Mole fraction of species I in stream k |

# Greek symbols

| | |
|---|---|
| $\alpha$ | Net water flux per proton flux |
| $\alpha_a$ | Anode transfer coefficient |
| $\alpha_c$ | Cathode transfer coefficient |
| $\beta_\xi$ | Permeability in the direction |
| $\varepsilon$ | Porosity of gas diffusion layer |
| $\eta$ | Overpotential for oxygen reaction [V] |
| $\lambda$ | Water content in the membrane |

| | |
|---|---|
| $\mu$ | Dynamic viscosity [kg s $m^{-2}$] |
| $\rho_{m,dry}$ | Density of a dry membrane [kg $m^{-3}$] |
| $\rho$ | Density of the mixture [kg $m^{-3}$] |
| $\sigma_m$ | Membrane conductivity [$\Omega^{-1}$ $m^{-1}$] |

# Subscript and Superscript

| | |
|---|---|
| $a$ | Anode |
| $c$ | Cathode |
| $e$ | Electrochemical reaction |
| $H_2$ | Hydrogen |
| $e$ | outlet |
| $N_2$ | nitrogen gas |
| $O_2$ | nitrogen gas |
| $p$ | phase change |
| $v$ | vapor |
| $w$ | water |
| $sat$ | saturated |
| $\xi$ | dummy variable for direction x, y, or z |

# Chapter 1. Introduction

## 1.1 Background of the study

Polymer electrolyte membrane fuel cells (PEMFCs) have been suggested as an alternative energy source by their high efficiency, high energy density, low noise level, and eco-friendly exhaust. Additionally, PEMFCs have the quick startup/shutdown characteristic and thus it can be applied excellently to dynamic vehicles including military purpose. PEMFC commonly consists of membrane-electrode assemblies (MEAs), gas diffusion layers (GDLs), bipolar plates and end plates.

GDLs play important roles that include reactant gas transportation, electron conduction, liquid water management and structural supporting of MEA. The GDLs typically consist of a micro-porous layer and a macro-porous layer. The macro-porous layer has anisotropic characteristics by preferential direction of mechanical properties. The GDL anisotropy can be divided into the anisotropy between in/through-plane and in-plane anisotropy. The in-plane anisotropy of GDL has both fiber directions that is perpendicular (designated by 90° GDL) and parallel (designated by 0° GDL) to the major flow when fuel cell components are assembled. Mechanical bending stiffness

according to the anisotropy is also different at each GDL. The different bending stiffness can cause different deformation characteristics when external force is applied. When fuel cell is assembled, the external compression force is applied to anisotropic GDL and degree of the deformation may be appeared differently. By this different deformation, contact resistances, pressure distributions and crossover rates between cell channels are distinguishable between 0° and 90° GDL.

Automotive PEMFCs experience relative humidity (RH) very frequently because they have dynamic operating characteristics. The repetitive RH variation induces frequent swelling/shrinkage of membrane, resulting in high mechanical stresses in the MEA. Due to this repetitive membrane swelling/shrinkage, contact between GDL and MEA under may become weaker and thus contact resistance of fuel cell can be reduced. Accordingly, it is estimated that fuel cell durability by different GDL bending stiffness of 0° and 90° GDL will be appeared differently.

In this study, fuel cells with 0° and 90° GDL are prepared to analyze cell performances and durability by anisotropic characteristics of GDL. Measurement of high frequency resistances (HFRs), I-V performance and pressure differences between cell inlet and outlet were carried out for identifying the effect of GDL anisotropy on cell performance in open mode of

which the outlets of both anode and cathode are opened. In addition, the purge characteristics of dead-end mode fuel cell were also investigated according to GDL anisotropy. Also, performances by in-plane crossover between channels were investigated by computational fluid dynamics (CFD). Next, wet/dry cycle method was used to analyze the effects of GDL anisotropy on cell degradation. HFRs, I-V performances and hydrogen crossover rate through the membrane were measured every 500 cycles. Above results were supported by morphological observation of GDL deformation.

## 1.2 Literature survey

GDL experiences deformation by clamping pressure when fuel cell components are assembled. This GDL deformation can influences on fuel cell performances. Ge et al. [1] investigated the effects of GDL compression on the performance of a PEMFC. They measured cell performances at different compression ratios using two types of GDL and the experimental results show that there exists an optimal compression ratio having maximum cell performance. Zhou et al. [2] reported that both the clamping force and the contact pressure distribution determine the contact resistance influencing the cell performance. They found that a larger clamping force and wider rib lead to a smaller contact resistance by numerical model. Chi et al. [3] studied numerically the effects of GDL compression on distribution of temperature, heat flux and consequently cell performance.

GDL have anisotropic characteristics between in-plane and through-plane. Many studies were conducted to analyze the effects of GDL anisotropy on thermal conductivity [4-7], diffusivity [8], permeability [9-11], electrical resistivity [12]. Also, mechanical properties according to the GDL anisotropy were studied. Kleemann et al. [13] reported that mechanical properties of the several type anisotropic GDLs were appeared differently. Serincan et al. [14]

investigated the effects of GDL anisotropy on the stress distribution in a PEMFC. They studied numerically that each of the in-plane and through-plane variations of the water content has a different effect on the deformation of membrane. In comparison with much studies of GDL anisotropy between in-plane and through-plane, there have been a few researches to study the effects of the in-plane anisotropy between machine direction (MD) and cross-machine direction (CMD) of GDL on cell performance. Naing et al. [15] reported that the cell performances with 90° GDLs were higher than those with 0° GDLs because 90° GDLs have superior ability for water removal than that of 0° GDLs. Han et al. [16] investigated the effects of GDL in-plane anisotropy on fuel cell performance using metallic bipolar plate with parallel flow fields. They found that performances of stacks with 90° GDL were higher than those with 0° GDL due to smaller intrusion into the gas channel, resulting in lower contact resistance values.

In the meantime, fuel cell is classified into open mode and dead-end mode according to opening and closing of outlets of both anode and cathode. The most studies have been focused on open mode fuel cell because of the higher applicability in automotive and stationary. Nevertheless, some studies about dead-end mode fuel cell have been conducted because that has many merits such as lower pressure drop, no air supply power consumption and

high system efficiency. In particular, it is very effective at underwater time of a submarine or flying time of an aerospace system by no exhausted gas. In this dead-end mode, performance reduction by water accumulation is critical issues because the liquid water accumulated at channel and GDL prevent efficient diffusion of reactant gases. Moçotéguy P et al. [17] studied the dynamic behavior of a five cells stack by experiments and numerical simulations. They reported that oxygen pressure at the GDL/electrode interface decrease rapidly due to increase in water accumulation of the stack. Purge process is an essential part in the dead-end mode fuel cell by water liquid accumulated in channel and GDL. Therefore, studies to reduce fuel wasted by purge process of dead-end mode fuel cell have been conducted. Choi et al. [18-19] investigated the effects of pulsation flow on purge characteristics of anodic and cathodic dead-end mode using visualized single fuel cell. They found that the pulsation flow augment the mean purge interval of the fuel cell by uniform water diffusivity. Sasmito et al. [20] studied performance degradation of anodic dead-end mode fuel cell by hydrogen depletion and water accumulation using transient model. They found that purging can maintain stable cell performance in anodic dead-end mode by release of the accumulated gas. The purge characteristics can be also influenced by GDL structure because water generated at catalyst layer is

transported to channel through the GDL. Thus, more experiments about the effects of GDL structure on dead-end mode fuel cell are needed.

Numerical studies to analyze the GDL anisotropic characteristics were conducted. Pasaogullari et al. [5], Serincan MF et al. [14], Ju et al. [21], Wu R et al. [22] and Yang WW et al. [23] developed model to analyze the GDL anisotropic characteristics between in-plane and through-plane. Researches about GDL in-plane anisotropy have been also conducted. He et al. [24] developed a three-dimensional and two-phase model to investigate the effect of the anisotropic GDL on the heat transfer and liquid water removal. They found that the thermal conductivity of GDL that is perpendicular to the gas channels produced the larger temperature difference than that of along channels.

For successful commercialization of PEMFCs, durability should be improved. Within the last several decade years, several studies have been published in regards to durability of PEMFCs for reaching the target lifespan according to Department of Energy (DOE) protocols for automotive applications (5000h) [25]. Also, for evaluating the durability of fuel cell, accelerated stress tests (ASTs) have been widely suggested because steady-state lifetime tests can be required very long time and high cost. So, many studies about ASTs have been conducted to assess the durability of PEMFCs

[26-31]. Startup/shutdown, freeze/thaw and wet/dry cycling are most commonly used AST methods for simulating the automotive vehicles. The startup/shutdown cycling has been used to simulate real road driving conditions for automotives. Reiser et al. [32] show a mechanism that may cause accelerated performance decay of fuel cell during startup/shutdown of power plant. Lee et al. [33] studied the effects of hydrogen removal during the idle period on cell performance and MEA degradation with repetitive loading cycle including purging. Eom et al. [34] investigated the effects of anode Pt loading on the degradation of MEA under reverse current conditions. The freeze/thaw cycling has been used to identify MEA durability under low temperature circumstances of subzero. McDonald et al. [35] studied the impact of freeze/thaw cycling on Nafion 112 membranes by ex-situ experiment. Lim et al. [36] investigated the effect of different GDL on freeze/thaw condition durability in PEMFCs. Zhang et al. [37] studied the degradation mechanism of the structure of MEA based on porosity and SEM measurement. The wet/dry gas supplying method was used for evaluating the degradation by membrane swelling/shrinkage. It is due to that the automotive PEMFCs have dynamic operating characteristics and thus experiences RH variation very frequently. The repetitive RH variation can induces frequent swelling/shrinking of membrane resulting in high mechanical stresses in the

membrane electrode assemblies. Huang et al. [38] reported that RH cycling significantly reduces the ductility of the Nafion-based MEA. Tang et al. [39] investigated the effects of the RH cycling on the mechanical breach and failure after 3000 cycles. They found that the stress generated by swelling/shrinkage of membrane is responsible for the mechanical decay of the Nafion PEMs. Kang et al. [40] investigated that wet/dry cycling reduced the performance of cell significantly and increased hydrogen crossover through the membrane because of the degradation of MEA. As illustration in Ref. [14], swelling of membrane can influence on the mechanical property and stress distribution of PEMFCs. The frequent swelling/shrinkage of membrane by dynamic operation of automotive can be different by this GDL in-plane anisotropy because different resistances of GDLs to repetitive swelling/shrinkage of membrane can be appeared according to the anisotropic GDLs.

## 1.3 Objectives and scopes

Experimental and analytical studies on the GDL anisotropy conducted extensively because it is directly related to the cell performance and durability. However, most of the studies focused on anisotropic characteristics between in-plane and through-plane, while there were not enough studies in in-plane anisotropic characteristics. The objective of present study is to investigate the effects of GDL in-plane anisotropy on cell performance under various operational and structural conditions. Furthermore, degradation rates of fuel cell with anisotropic GDLs were compared during wet/dry cycles.

In chapter two, the experimental setup and test conditions were presented. Preparation of the test station, single fuel cell, auxiliary components such as fuel supply system, humidifying system, devices for measurement and hydrogen crossover measurement system was shown. Especially, specifications of specially-designed GDL of carbon felt-type were introduced.

In chapter three, the results of cell performances, HFRs and air pressure differences by GDL in-plane anisotropic directions were compared under various channel/rib width ratio. Also, purge characteristics of cathodic dead-end mode according to GDL anisotropy were investigated. Morphological images of the anisotropic GDL deformation were analyzed by digital

microscope.

In chapter four, numerical works using computational fluid dynamics (CFD) code are conducted for analyzing gas transfer characteristics in anisotropic GDLs. Mesh grids were generated considering the different deformations of anisotropic GDLs.

In chapter five, the effects of GDL in-plane anisotropy on durability of fuel cells during wet/dry cycles were shown. Cell performances, HFRs and hydrogen crossover rates of fuel cell with anisotropic GDLs were compared. Morphological images were analyzed by scanning digital microscope (SEM) for identifying degrees of the anisotropic GDL degradation.

Finally, brief summarization of results and discussions were given.

# Chapter 2. Experimental apparatus and method

## 2.1 Introduction

Fig. 2.1 shows schematic diagram of the experimental setup used in this study. The experimental setup can be divided by fuel supplying, humidification and temperature controlling system. Hydrogen with the purity of 99.999% and the air are used for the reaction of fuel cell.

## 2.2 Single fuel cell

In this study, a single fuel cell composed of the membrane electrode assembly (MEA), gas diffusion layers (GDLs), bipolar plates with a 5-serpentine channel for both anode and cathode flow fields, gaskets and end plates was used. A commercially-available perfluorinated sulfonic acid MEA with an active area of 25 $cm^2$ was used. Both the anode and cathode of an MEA were composed of typical Pt/C catalysts, and the Pt loadings of the anode and cathode were both 0.4 mg Pt $cm^{-2}$. Thickness of GDL samples was 276 ± 6 μm, the average of 100 measurements with a Mitutoyo thickness gauge (KWC 576 model, Mitutoyo Co., Japan). The model GDL was used to analyze GDL anisotropic characteristics certainly and the properties according

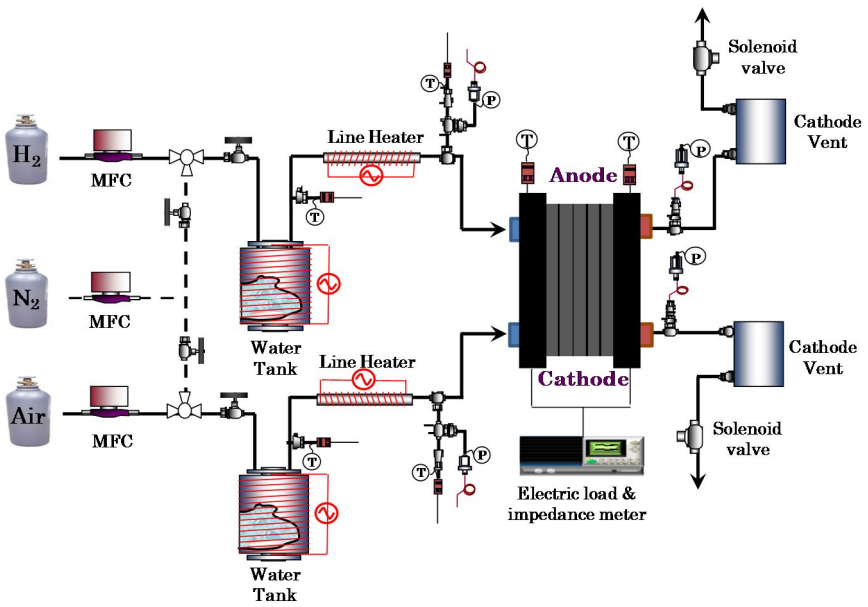


**Fig. 2.1** Schematic diagram of the experimental setup

to machine and cross-machine directions are summarized in Table 2.1. The surface morphology of macro-porous substrate and micro-porous layer (MPL) were observed by Digital Microscope (AM-413T5, Dino-Lite, Taiwan) at a magnification of 100×. The macro-porous substrate of the GDL samples was made by carbon fiber felt having in-plane anisotropic characteristics. As shown in Fig. 2.2(a) and (b), the macro-porous substrate and MPL shows typical structure observed in most commercial GDLs. A torque wrench was used for uniform assembly of fuel cell and the torque wrench was set at 7.9 N m. A leakage test was performed for checking the sealing condition of fuel cell components after the assembly of the fuel cell.

## 2.3 Experimental apparatus and test conditions

All reactants were controlled by mass flow controllers (Bronkhorst High-Tech, the Netherlands). The reactants were humidified by the heated water in bubbler type humidifier, of which the water temperatures controlled by heaters in the humidifier. The due point temperature was measured at outlet of humidifier by chilled mirror type hygrometer (Yamadake, FDB). T-type thermocouples (TC) with an uncertainty of ±0.5 $^{o}$C were used to measure temperatures of supply gases and fuel cell unit. Line heaters covering from the

**Table 2.1** Characteristics of the GDLs used in this study.

| **properties** | Machine direction (MD) | Cross-machine direction (CMD) |
|---|---|---|
| Substrate | Carbon fiber-felt | |
| Thickness | 276 ± 6 $\mu$m | |
| In-plane electrical conductivity | 41.27 ± 0.26 S/cm | 21.20 ± 1.42 S/cm |
| Bending stiffness / Taber stiffness unit | 19.37 ± 1.28 $g_f \cdot cm$ | 0.42 ± 0.02 $g_f \cdot cm$ |

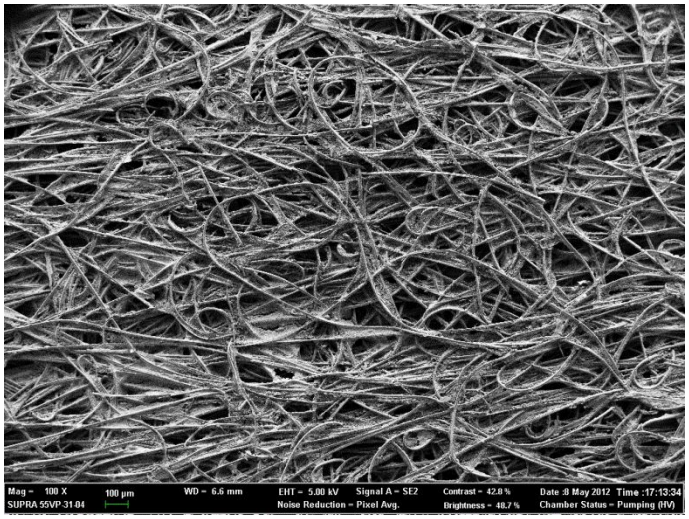


**(a) macro-porous substrate**

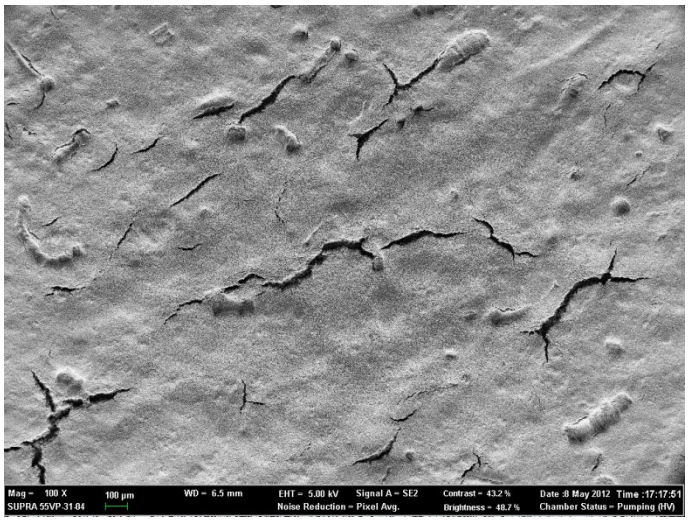


**(b) micro-porous layer**

**Fig. 2.2** Surface morphologies of the GDLs: (a) macro-porous substrate and (b) micro-porous layer.

mass flow meter outlet to fuel cell inlets controlled the supply gasses. The holes of the thermocouple were inserted into a long hole of 40 mm depth in both the anode and cathode bipolar plates and located 10 mm away from the center line of bipolar plates. The temperature of cell was controlled by cartridge heaters inserted into of both anode and cathode end plates. All the temperatures of fuel supplying line, humidifiers and cells are adjusted by PID controller. The gas pressures of both the anode and cathode sides were monitored by pressure transducers with an uncertainty of ±0.15%. For operating fuel cell by cathodic dead-end mode, the solenoid valves were installed at the cathode outlet. The solenoid valves are closed initially and are fully open the purge process for discharging the liquid water generated by fuel reaction. When the cell voltage drop to reference voltage set to protect the fuel cell, purge is started automatically until the voltage is recovered. An electric loader (PLZ 1004WA, Kikusui Electronics, Japan) was used to measure single fuel cell performance and HFR). As shown in Fig. 2.3, mass spectrometer (Hidden Analytical, Warrington, UK) used the hydrogen crossover rate in cathode side channel. A flushing sequence was used to eliminate the residual oxygen and nitrogen in the ambient air for at least three hours. The experimental data was collected by data acquisition system and a computer. For acquiring all the outputs from the measuring equipments, multi-channel


**Fig. 2.3** The picture of the mass spectrometer system used in this study.

recorder was installed and the computer is realized via GPIB interface. An activation process was conducted for 10 h to activate the fresh fuel cell before experiments under cell temperature of 65$^{o}$C, ambient pressures, RH of 100%/100% and stoichiometric ratios of 1.5/2.0.

# Chapter 3. Cell performances by GDL anisotropic characteristics

## 3.1 Introduction

The structure of GDL is deformed when the cell components are assembled as shown Fig. 3.1. The deformation leads to GDL intrusion into the gas channel and reduction of GDL porosity. As mentioned earlier, the roles of the GDL are very relevant to fuel cell performance. When the GDL is mechanically compressed by assembly of cell components, the strength for mechanical supporting between bipolar plates and MEA is weakened and the GDL porosity is reduce. These effects can be appeared differently by the GDL in-plane anisotropy. Therefore, characteristic differences such as electrochemical performances, pressure difference and contact resistances between fuel cells with 0° and 90° GDLs need to be studied in open mode. Also, liquid water in GDL takes an important role in dead-end mode fuel cell. The liquid water imposes purge process exhausting the liquid water to outlet using supplying gas in order to transporting smoothly fuel to catalyst layer. Therefore, the deformation and porosity reduction of anisotropic GDLs can influence on the purge characteristics. To clarify this speculation, the purge

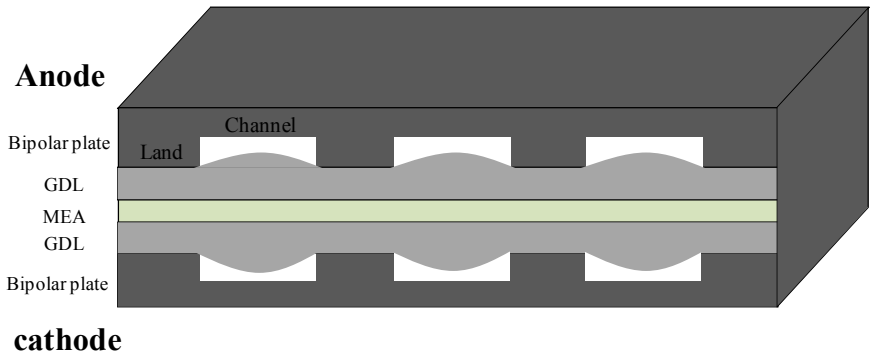


**Fig. 3.1** Schematic diagram of cross-sectional fuel cell showing GDL intrusion and deformation.

characteristics of dead-end mode fuel cell according to GDL anisotropy also need to be studied.

## 3.2 Performance tests in open mode fuel cell

Deformation and intrusion of 0° and 90° GDLs is different when the GDL is compressed by the land part of bipolar plates because of the different directions of mechanical strength. Therefore, differences according to geometries of land and channel parts of bipolar plates can be also appeared. Therefore, we focused the differences of cell performance by GDL anisotropy and the tendency according to geometry of bipolar plates in this study. The present study examined the effects of GDL anisotropy on electrochemical performances and pressure differences. The geometrical characteristics of the bipolar plates used in the measurements of the open mode fuel cells were summarized in Table 3.1.

### 3.2.1 I-V performances

Fig 3.2 shows the polarization curve of the cell with 0° and 90° GDLs in the open mode operation for different bipolar plates (BP-1, 2 and 3) at RH of 100%/100% and operation temperature of 65°C conditions. The BP-1, 2 and 3

**Table 2.1** Characteristics of the GDLs used in this study.

| BP code | Land width (mm) | Channel depth (mm) | Channel depth (mm) | |
|---|---|---|---|---|
| | | | anode | cathode |
| BP-1 | 0.38 | 1.42 | 0.4 | 0.6 |
| BP-2 | 0.75 | 1.05 | 0.4 | 0.6 |
| BP-3 | 1.12 | 0.68 | 0.4 | 0.6 |
| BP-4 | 0.38 | 1.42 | 0.2 | 0.2 |
| BP-5 | 0.38 | 1.42 | 0.6 | 0.6 |
| BP-6 | 0.38 | 1.42 | 1.0 | 1.0 |

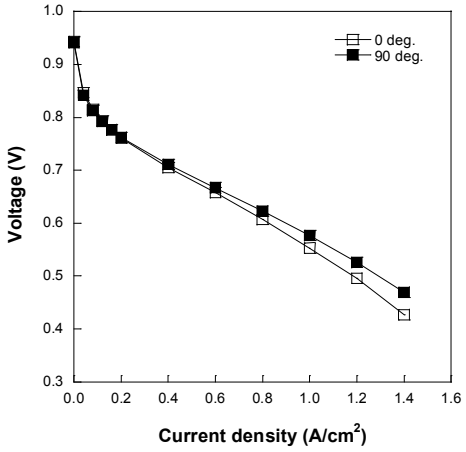


**(a) BP-1**

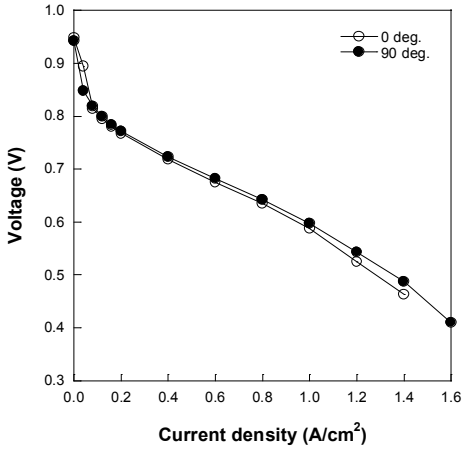


**(b) BP-2**

**Fig. 3.1** Electrochemical I-V performances of fuel cells with 0° and 90° GDLs as a function of land/channel width ratio.

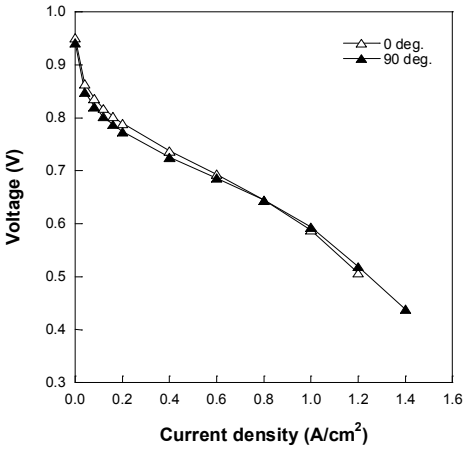


**(c) BP-3**

**Fig. 3.1** Electrochemical I-V performances of fuel cells with 0° and 90° GDLs as a function of land/channel width ratio (continued).

have land/channel width ratio of 0.27, 0.71, and 1.65, respectively. The performance of fuel cell with 90° GDL is higher than that of 0° GDL in all BPs. The fuel cell with 90° GDL and BP-1, which has the land/channel width ratio of 0.27 has higher performance than that with 0° GDL and BP-1 as shown in Fig 3.2 (a). The voltage difference between the fuel cells with 0° and 90° GDL in low current density under 0.4 A/cm$^2$ is negligible. In high current density, the voltage difference becomes higher. The fuel cells with BP-2 have higher performance than those with BP-1 under overall current densities due to wider contact surface between GDL and land part of bipolar plate. The voltage difference between the fuel cells with 0° and 90° GDLs at high current density was smaller than case of BP-1, implying that the deformation and intrusion into channel of GDL with narrower land width is more severe. As the land/channel width ratio increases up to 1.65, the difference of I-V performances between the 0° and 90° GDLs cells were very small, indicating that the land of bipolar plate over certain width sufficiently support GDL and thus deformation difference by cell assembly is negligible. Fig 3.3 shows cell voltage variation of fuel cells with 0° and 90° GDLs for different land/channel width ratios. While the voltage of BP-3 is higher than that of BP-1 and BP-2 in low current density of 0.4 A/cm$^2$, the voltage of BP-3 is lower than that of BP-2 in high current density of 1.2 A/cm$^2$. The wider land width stably

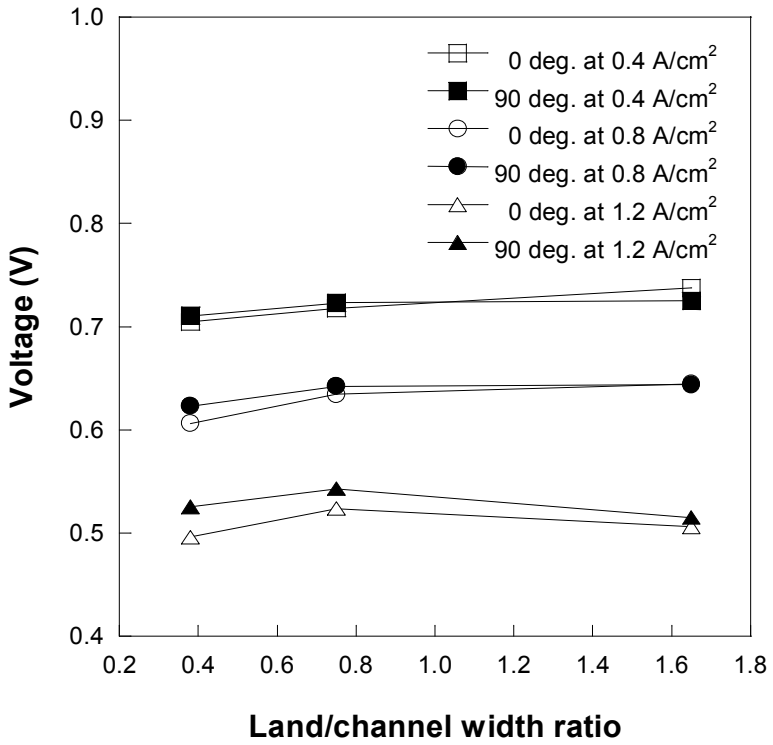


**Fig. 3.3** Cell voltage variation of fuel cells with 0° and 90° GDLs at 0.4, 0.8 and 1.2 A/cm$^2$ as a function of land/channel width ratio.

support the GDL, but the wider land width, meaning the narrower channel width leads to reduction of volume for mass transport. Due to these competing factors, the optimum ratio of land/channel width can be found.

Fig. 3.4 shows the electrochemical I-V performance of fuel cells with 0° and 90° GDLs for different channel depths at same operating temperature and RH as Fig. 3.2. BP-4, 5 and 6 have channel depths of 0.2/0.2, 0.6/0.6 and 1.0/1.0, respectively at anode/cathode side. The voltages of all the fuel cells with 90° GDLs in BP-4, 5 and 6 were higher than those of fuel cells with 0° GDLs. However, the differences between fuel cells with 90° GDLs and 0° GDLs were appeared in the BP-4, 5 and 6 as shown in Fig 3.5. For instance, the voltage difference of BP-4, 5 and 6 at 1.2 $A/cm^2$ was 0.037, 0.0575, and 0.055 V, respectively. The difference of the BP-4 was lower than the others implying that effect of anisotropic bending stiffness of the GDLs increase till specific point, but not over the point. This means that prevention of mass transport by channel intrusion of the GDLs is negligible over critical channel depth.

### 3.2.2 High frequency resistances

As mentioned above, when the fuel cell components are assembled, the

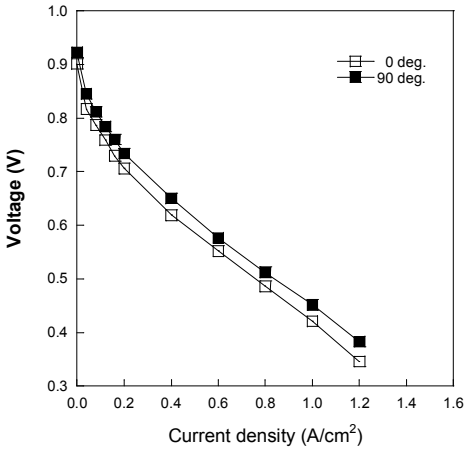


**(a) BP-4**

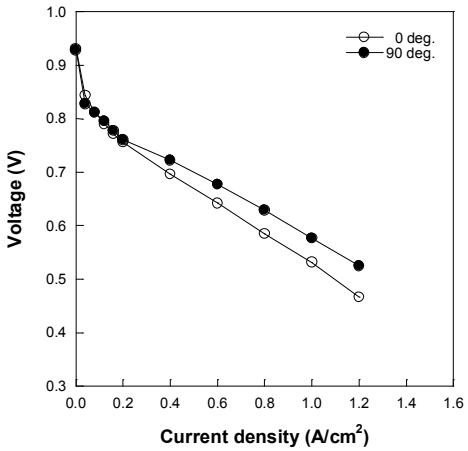


**(b) BP-5**

**Fig. 3.4** Electrochemical I-V performances of fuel cells with 0° and 90° GDLs as a function of channel depth.

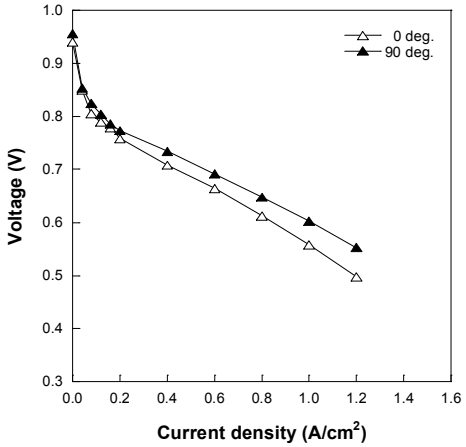


**(c) BP-6**

**Fig. 3.4** Electrochemical I-V performances of fuel cells with 0° and 90° GDLs as a function of channel depth (continued).

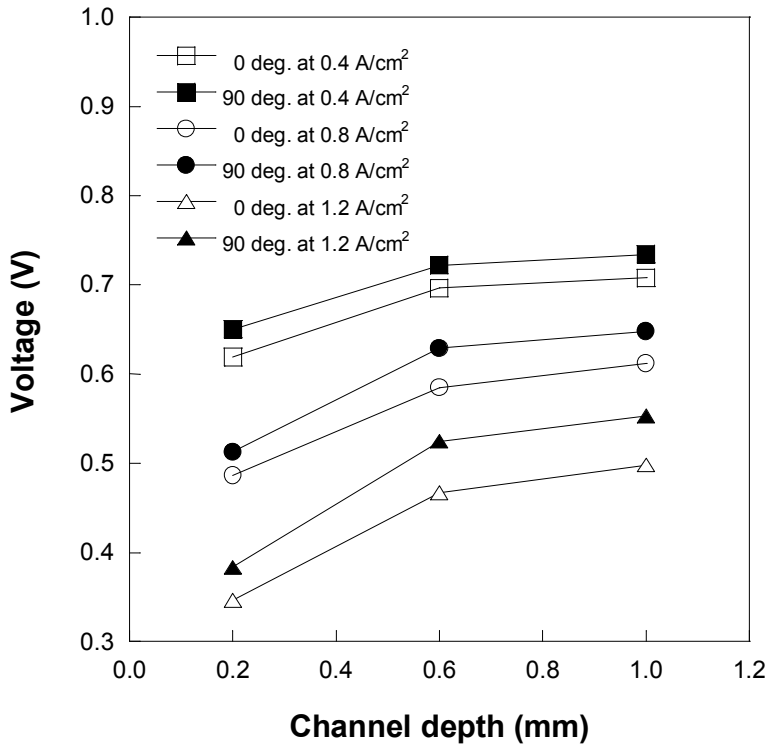


**Fig. 3.5** Cell voltage variation of fuel cells with 0° and 90° GDLs at 0.4, 0.8 and 1.2 A/cm$^2$ as a function of channel depth.

carbon fibers of GDLs deformed and intrude into channel by the force from land part of bipolar plates. This damaged carbon fibers cause to the increase of contact resistance meaning the reduction of cell performance. HFR has been often used to measure the electrical contact resistance associated with the interfaces between various fuel cell components. For clarifying differences of contact resistance according to GDL anisotropy, the HFRs of the 0° and 90° GDLs fuel cells were measured in same BP conditions as Chap. 3.2.1. Fig. 3.6 shows HFRs with 0° and 90° GDLs for different bipolar plates (BP-1, 2 and 3) at RH of 100%/100% and operation condition of 65°C conditions. The HFRs of all the fuel cells with 90° GDLs in BP-1, 2 and 3 were higher than those of fuel cells with 0° GDLs. These results indicate that the 90° GDL have higher mechanical resistance to the cell assembly and thus less damage than 0° GDL. The HFR differences between the fuel cells with the 90° and 0° GDLs of BP-1 were higher than the others as shown in Fig 3.7. It was confirmed that the effects of anisotropic bending stiffness of GDL on the deformations is highest at low land/channel width ratio. Fig. 3.8 shows the HFR differences of fuel cells with the 90° and 0° GDLs for different channel depths (BP-4, 5 and 6). The trend is similar with the Fig 3.7, but the HFR values of both 90° and 0° GDL cells with BP-4 were higher than those of cells with BP-5, 6 as shown in Fig 3.9. The results indicate that shallow channel volume of the BP-4 may

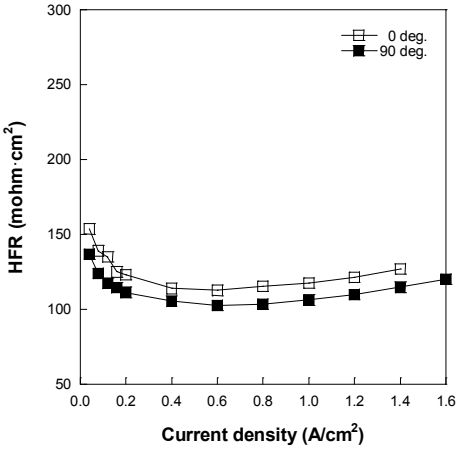


**(a) BP-1**

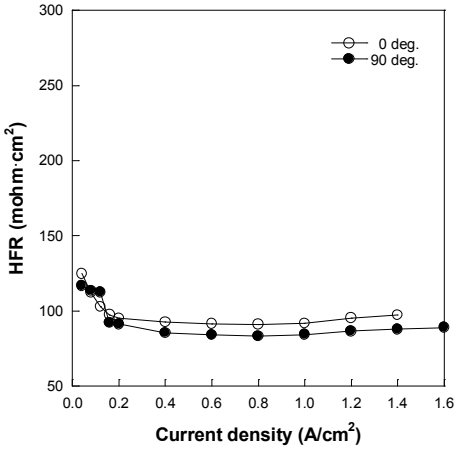


**(b) BP-2**

**Fig. 3.6** High frequency resistances of fuel cells with 0° and 90° GDLs as a function of land/channel width ratio.

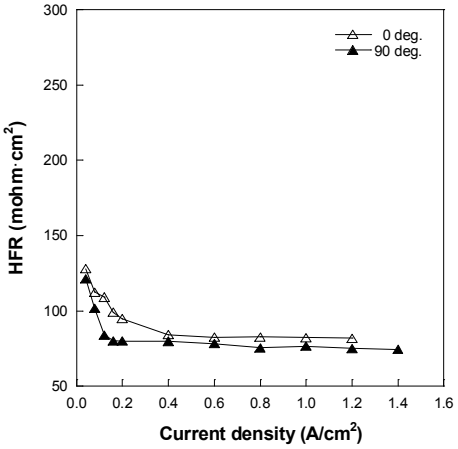


**(c) BP-3**

**Fig. 3.6** High frequency resistances of fuel cells with 0° and 90° GDLs as a function of land/channel width ratio (continued).

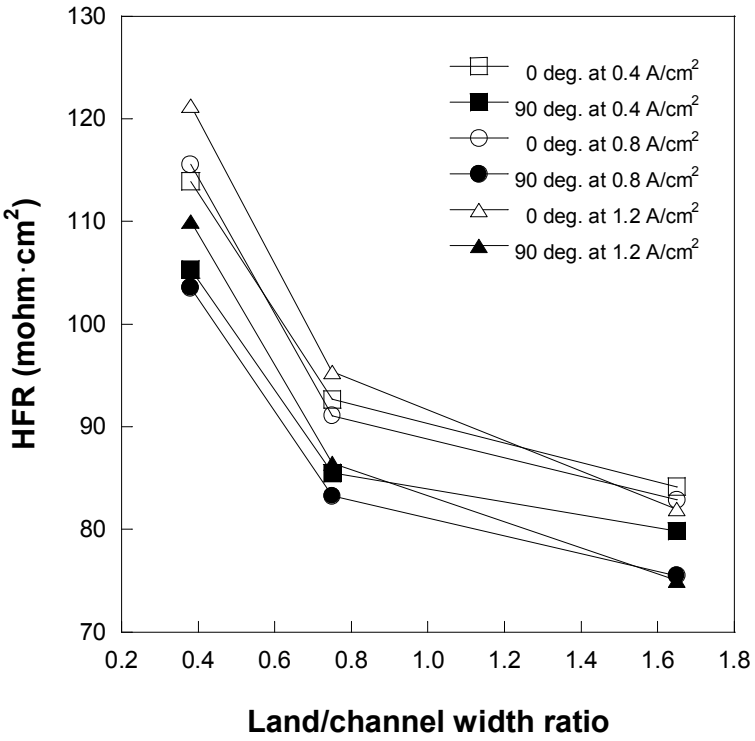


**Fig. 3.7** High frequency resistance variations of fuel cells with 0° and 90° GDLs at 0.4, 0.8 and 1.2 A/cm$^2$ as a function of land/channel width ratio.

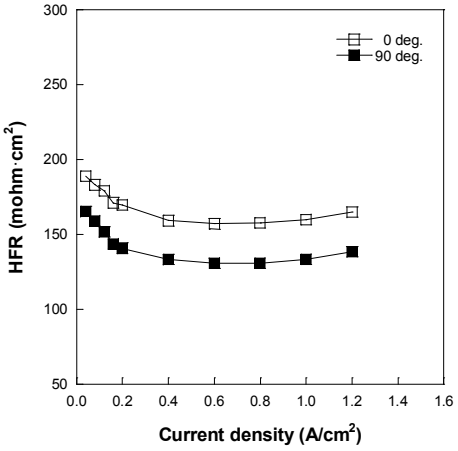


**(a) BP-4**

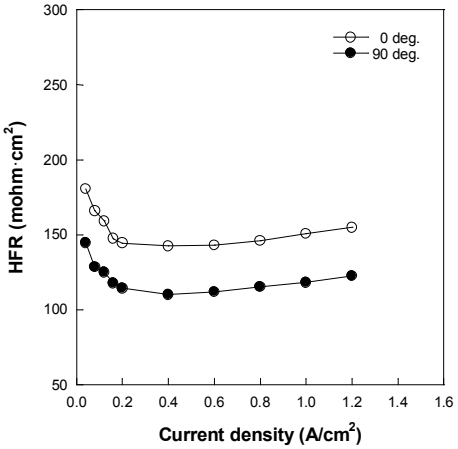


**(b) BP-5**

**Fig. 3.8** High frequency resistances of fuel cells with 0° and 90° GDLs as a function of channel depth.

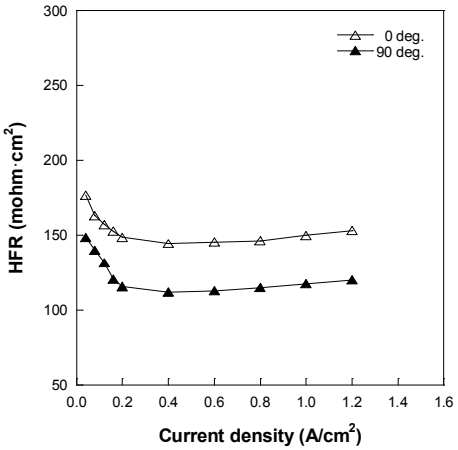


**(c) BP-6**

**Fig. 3.8** High frequency resistances of fuel cells with 0° and 90° GDLs as a function of channel depth (continued).

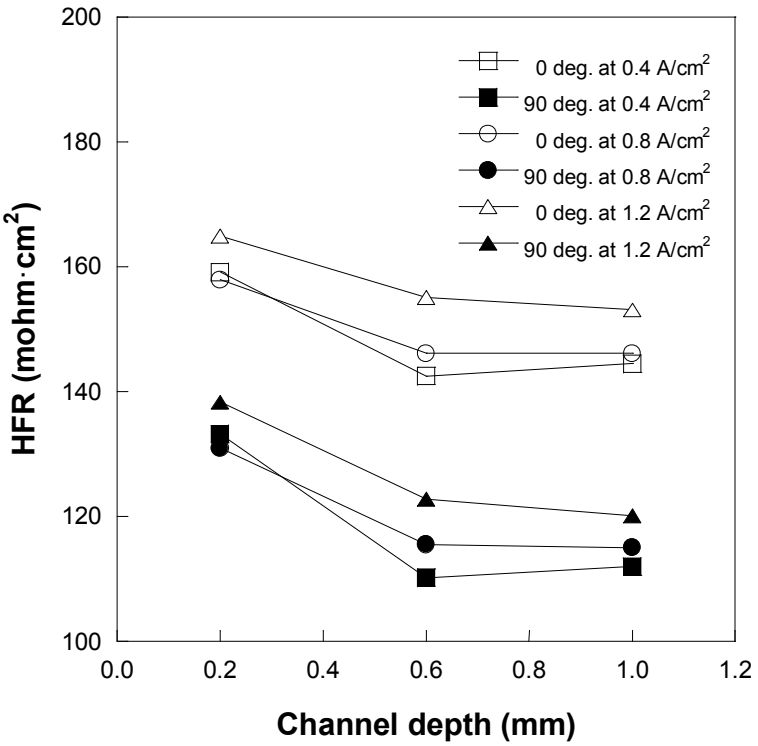


**Fig. 3.9** High frequency resistance variations of fuel cells with 0° and 90° GDLs at 0.4, 0.8 and 1.2 A/cm$^2$ as a function of channel depth.

induce the higher pressure in gas channel and thus contact status at the interfaces between the GDLs and land may also deteriorated.

### 3.2.3 Pressure differences

The variation of volume by channel geometry causes the gas $\Delta P$ between the inlet and outlet of fuel cell. Commonly, the $\Delta P$ in cathode side is higher than that in anode side because of higher stoichiometric ratio and nitrogen contained. In this study, air pressure differences of fuel cells were measured. Fig. 3.10 shows air pressure difference of fuel cells with the 90° and 0° GDLs for different land/channel width ratios. The gap of the air $\Delta P$ between fuel cells with the 90° and 0° GDLs is negligible for all the BPs implying that the contact resistance is dominant compared with mass transport in effects of GDL's anisotropic stiffness as shown in Fig 3.11. However, the air $\Delta P$ values increase significantly due to the smaller channel volume when the land/channel width ratio increases. Fig. 3.12 shows air $\Delta P$ values of fuel cells with the 90° and 0° GDLs for different channel depths. Difference of air $\Delta P$ between fuel cells with BP-1 has significantly higher than cells with the other BPs having almost no $\Delta P$ as shown in Fig. 3.13. These results indicate difference of channel intrusion between fuel cells with 90° and 0° GDLs was

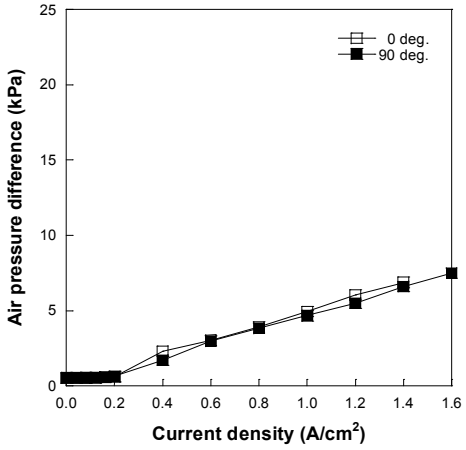


**(a) BP-1**

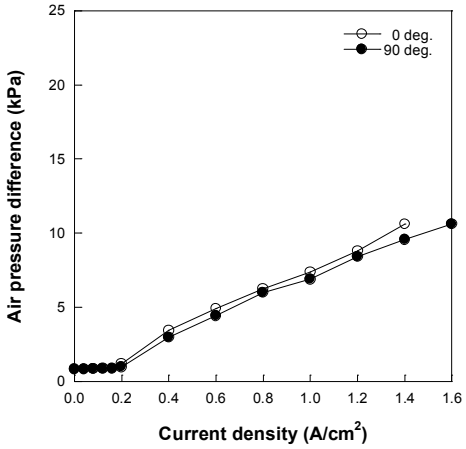


**(b) BP-2**

**Fig. 3.10** Air pressure difference of cathode of fuel cells with 0° and 90° GDLs as a function of land/channel width ratio.

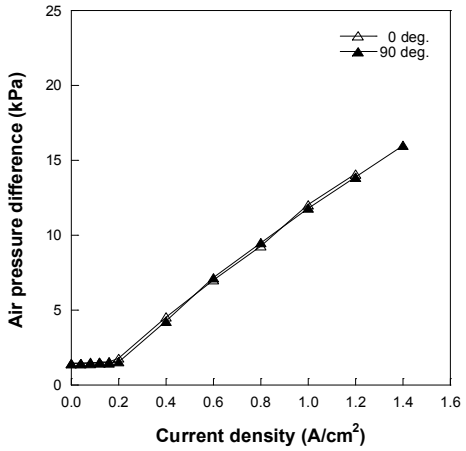


**(c) BP-3**

**Fig. 3.10** Air pressure difference of cathode of fuel cells with 0° and 90° GDLs as a function of land/channel width ratio (continued).

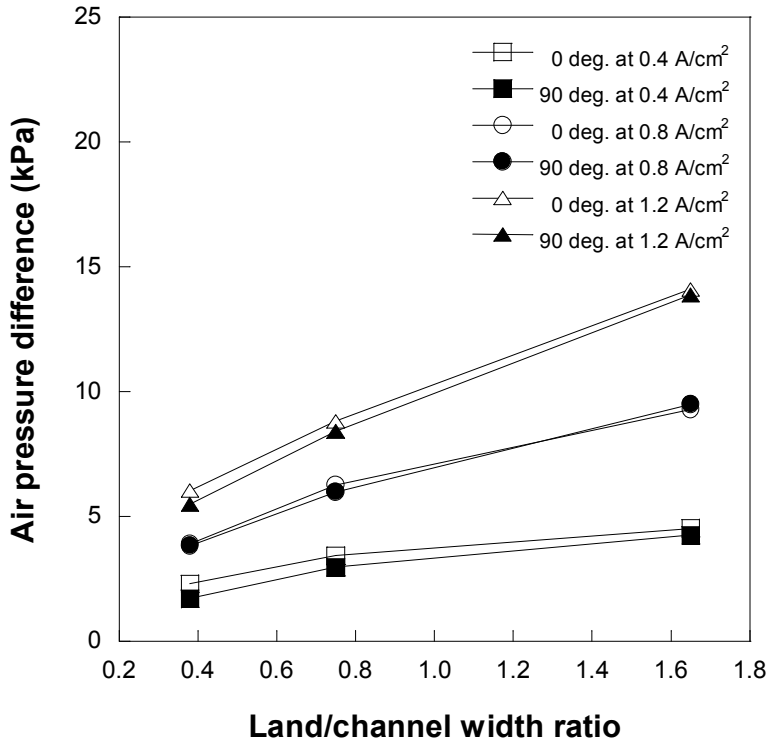


**Fig. 3.11** Air pressure difference variations of cathode of fuel cells with 0° and 90° GDLs as a function of land/channel width ratio.

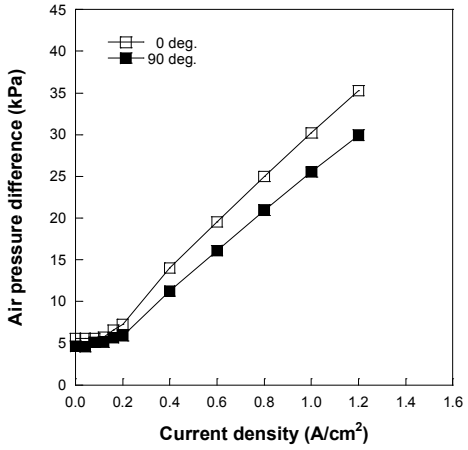


**(a) BP-4**

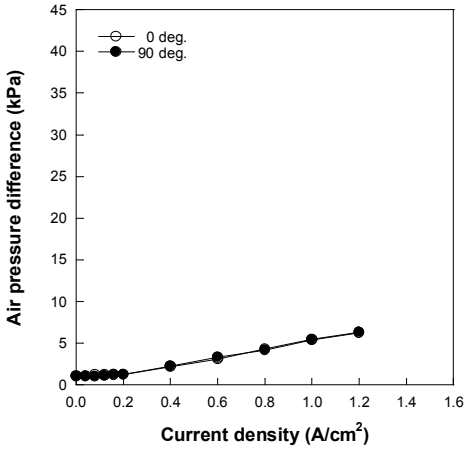


**(b) BP-5**

**Fig. 3.12** Air pressure difference of cathode of fuel cells with 0° and 90° GDLs as a function of channel depth.

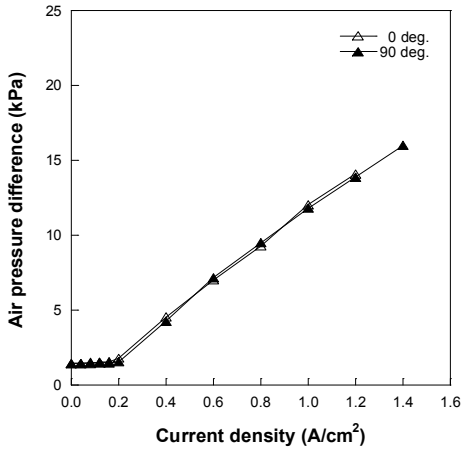


**(c) BP-6**

**Fig. 3.12** Air pressure difference of cathode of fuel cells with 0° and 90° GDLs as a function of channel depth (continued).

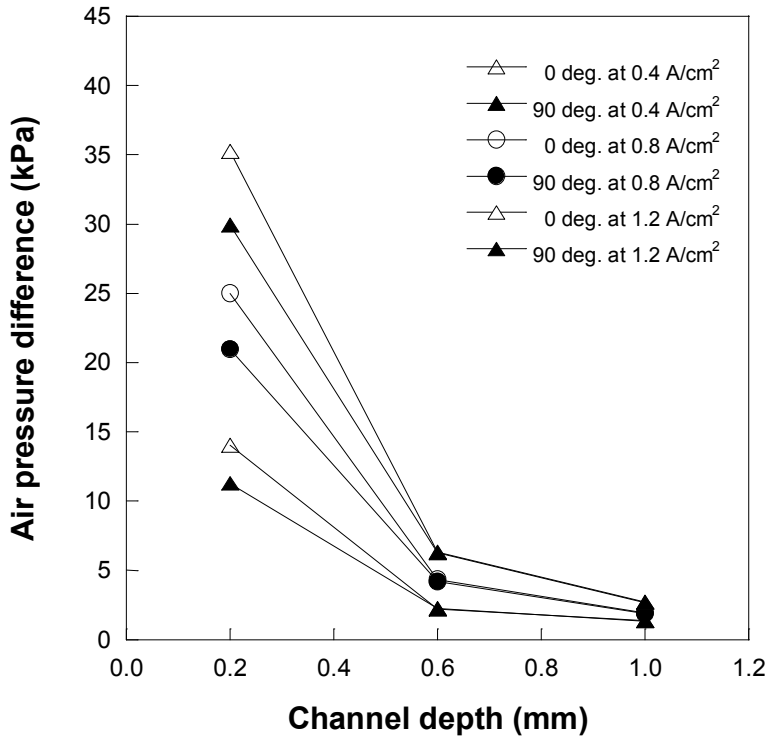


**Fig. 3.13** Air pressure difference variations of cathode of fuel cells with 0° and 90° GDLs as a function of channel depth.

not appeared in sufficient depth. This higher $\Delta P$ of MP-1 may lead to deterioration the contact status at the interfaces between the GDL and the land. Therefore, these results can support the measurements of HFRs having significant difference in BP-1.

### 3.2.3 Electrical resistances of bipolar plates

For analyzing the effect by the bipolar plates themselves, electric resistances of bipolar plates and GDLs were measured. Mock-ups of bipolar plates with different channel depths of 0.2 and 0.4 mm were prepared as shown in Fig 3.14. Fig. 3.15 shows experimental setup for measuring electric resistances of BPs. Compression pressures were measured by the pressure gauge and electric resistances were measured by the ohm-meter. GDL and bipolar plate were placed on the plate of the pressure gauge. Fig 3.16 shows electric resistances of bipolar plates with 0° and 90° GDL cell. Electrical resistance of 90° GDL cell is smaller than that of 0° GDL cell by the lower deformation of 90° GDL. The bipolar plate of 0.2 mm has higher electric resistance than the 0.6 mm bipolar plate indicating the higher volume of bipolar plate. This means that the volume and geometry of bipolar plate can influence on the cell performance.

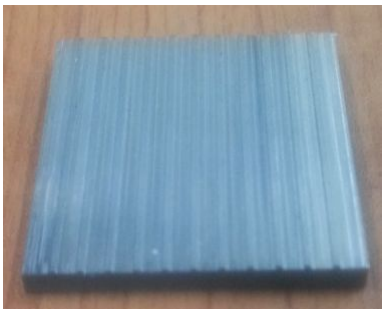

**(a) 0.2 mm**

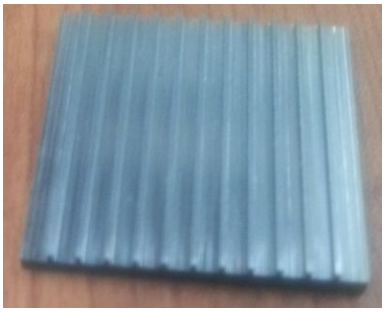

**(b) 0.6 mm**

**Fig. 3.14** Mock-up of bipolar plates with different channel depths.

**Fig. 3.15** Experimental setup for measuring electric resistances of BPs.

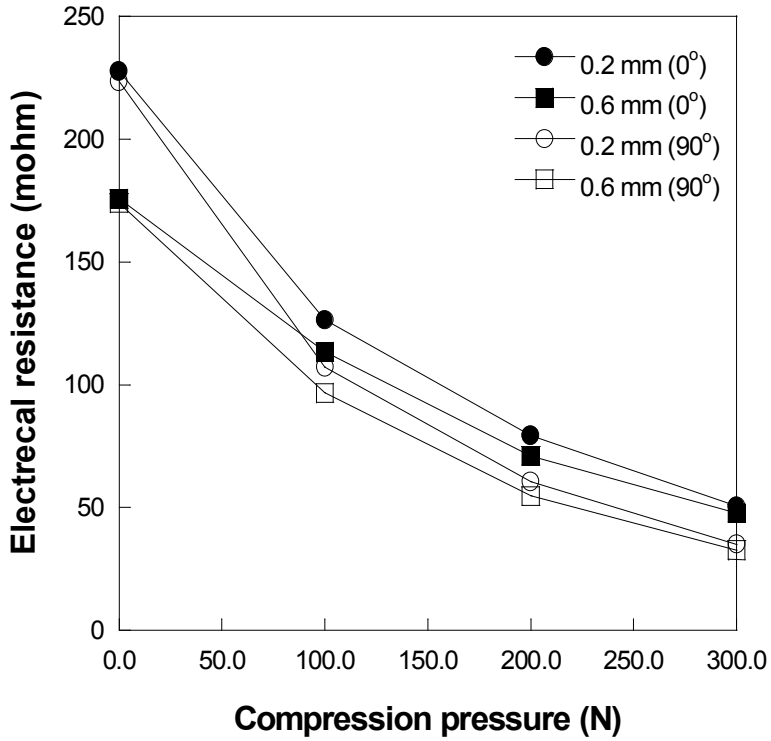


**Fig. 3.16** Electric resistances of bipolar plates with 0° and 90° GDL cell.

## 3.3 Performance test in cathodic dead-end mode fuel cell

In dead-end mode operation, fuel cell outlet is block and the operation pressure is controlled by a pressure regulator at inlet of fuel cell. Therefore, when fuels are reacted at MEA, liquid water is generated at cathode catalyst layer and diffuse to the cell channel through the GDL. Because the outlet dead-end mode fuel cell is blocked, liquid water in GDL gradually increases. So, reactants cannot efficiently diffuse into catalyst layer and accordingly, purge process that periodically remove the water liquid into outside of fuel cell is needed for continuous fuel reaction. The purge characteristic is changed by operation condition such as current density, operating temperature and pressure because variation of the operation condition influence on generation and transport of water liquid [18-19]. Also, the purge characteristic is changed by GDL material characteristics such as porosity and mechanical stiffness. Especially, the deformation by GDL anisotropic bending stiffness can reduce the GDL porosity and influence on the purge characteristics when fuel cell is operated by dead-end mode. In this section, purge interval of fuel cells with 90° and 0° GDL is measured for analyzing the effect of GDL anisotropy in dead-end mode.

### 3.3.1 Methods for experiments

Fig. 3.16 shows the schematics of dead-end mode fuel cell with gas regulator, mass flow controller and solenoid valve. For simulating the enclosed propulsion systems such as submarine and aerospace, pure oxygen is used. Initially, the solenoid valve is completely closed. After fuel cell start operation and the cell performance decrease to predetermined voltage by liquid water, the solenoid valve is fully open. For the closing time of the solenoid valve, the oxygen is supplied into the cathode channel as much as required to the reaction by pressure difference between the inlet and inside of the cell channel. When the voltage drop to the predetermined voltage, the purge is started flow for removing the liquid water in GDL and channel. The purge is finished when the cell voltage is recovered above the setting value.

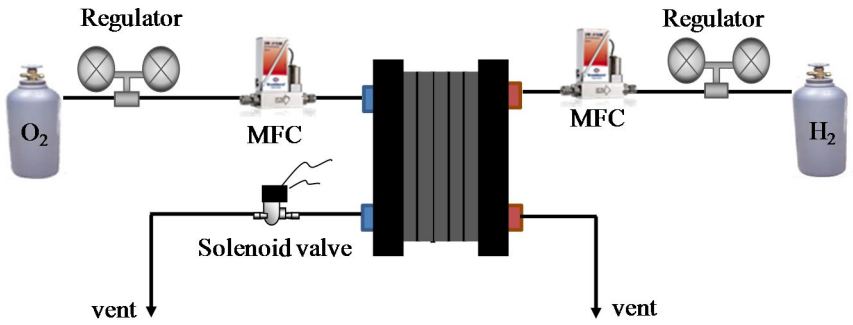


**Fig. 3.17** Configuration of the cathodic dead-end mode fuel cell operation.

The predetermined reference voltage is set at 15% off value of the maximum voltage because the voltage drop drastically from about 17~18% of the maximum voltage. The solenoid valve is operated automatically by Lab-View. The operating pressure of both the cathode and anode is controlled by pressure regulator attached on the oxygen and hydrogen tanks. The periodical purge intervals over 5 times were observed after stable operation. All experimental conditions for dead-end mode fuel cell are shown in Table 3.2.

### 3.3.2 Purge characteristics by GDL anisotropy

Fig. 3.17 shows variation of the dead-end mode fuel cell at 0.7 A/cm$^2$. The voltage dropped gradually until the purge process starts. After the purge process, the voltage increased sharply by removal of water liquid in GDL and channel. The peak voltage of the 0° GDL cell was also higher than 90° GDL indicating the higher contact resistance in 0° GDL cell. The purge interval of the fuel cell with 0° GDL was also longer than that of the fuel cell with 90° GDL. The result is caused by the difference of GDL porosity reduction between both to 90° and 0° GDL cells at same cell assembly pressure as represented in chapter 3.2.4. The more deformation of 0° GDL leads to more reduction of GDL porosity. In the condition of same water liquid, the water

**Table 3.2** Experimental conditions for the cathodic dead-end mode fuel cell.

| **Parameter** | **unit** | **Anode inlet** | **Cathode inlet** |
|---|---|---|---|
| Cell temp. | ℃ | 65 | 65 |
| Inlet temp. | ℃ | 65 | 65 |
| Pressure | Bar | 1.05 | 1.3 |
| Relative humidity | % | 100 | 100 |
| Stoichiometric ratio | - | 1.5 | - |
| Sampling time | s | 1.42 | 1.0 |
| Reference voltage for purging | V | 15% off value of maximum voltage | |

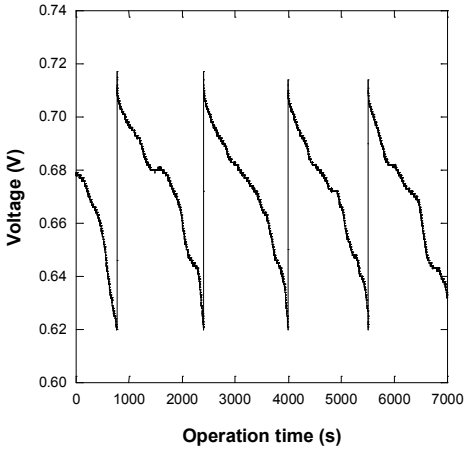


**(a) 0° GDL cell**

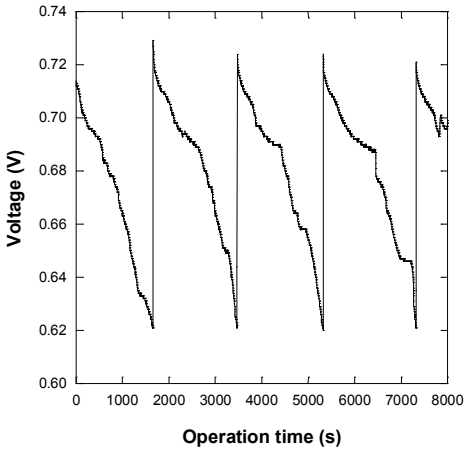


**(b) 90° GDL cell**

**Fig. 3.18** Variation of the cell voltage in dead-end operation at 0.7 A/cm$^2$.

liquid thickness in the 0° GDL is higher than that in the 90° GDL as expressed in Eqs. (3.1)

$$t_{wl} = \frac{m_{wl}}{\varepsilon \rho_{wl} Area} \tag{3.1}$$

where $t_{wl}$ is the water liquid thickness attached at GDL when it is assumed that the water liquid is distributed at GDL uniformly, $m_{wl}$ is mass of water liquid in GDL, $\rho_{wl}$ is the water liquid density, Area is the GDL's surface area and ε is GDL porosity. Accordingly, more porosity reduction of 0° GDL cause thicker water liquid in GDL and earlier drop of cell performance. When the current density increase, water is more rapidly generated at cathode catalyst layer and distributed as liquid in GDL. Therefore, the purge interval decreases at higher current density as shown in Fig. 3.18, 19. As Fig. 3.17, the peak voltage of the 0° GDL cell was higher than 90° GDL cell and the purge interval of that was shorter than 90° GDL cell. However, power generated for same time have to used for comparing the 90° and 0° GDL cell in dead-end mode reasonably. So, averaged voltages of 5 purge interval as a function of current density for same time were represented as Fig. 3.21. The voltages of 90° GDL cell were higher than those of 0° GDL cell and the difference is more obvious at higher current density owing to the higher contact resistance in the higher current density.

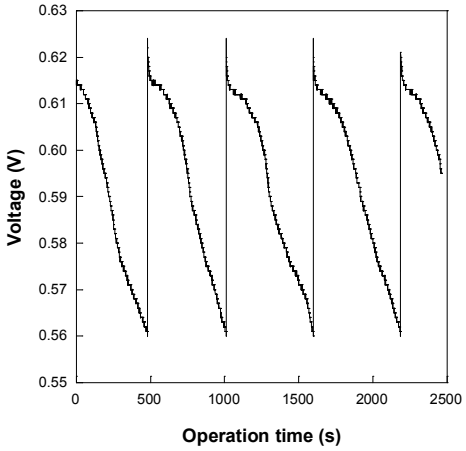


**(a) 0° GDL cell**

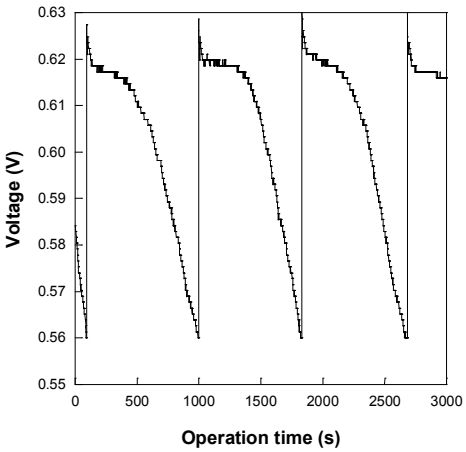


**(b) 90° GDL cell**

**Fig. 3.19** Variation of the cell voltage in dead-end operation at 1.0 A/cm$^2$.

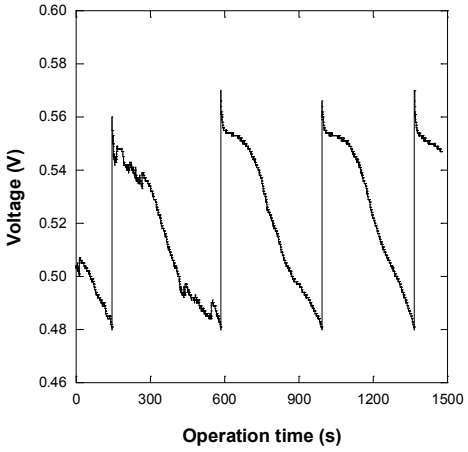


**(a) 0° GDL cell**

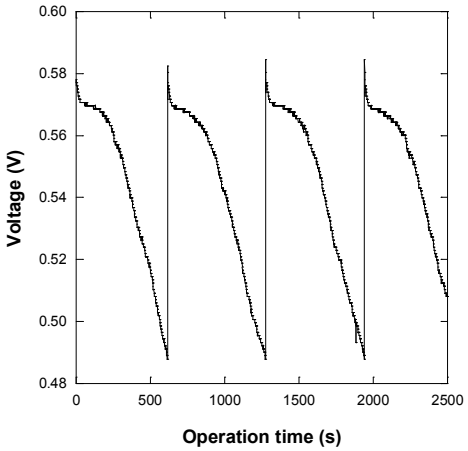


**(b) 90° GDL cell**

**Fig. 3.20** Variation of the cell voltage in dead-end operation at 1.3 A/cm$^2$.

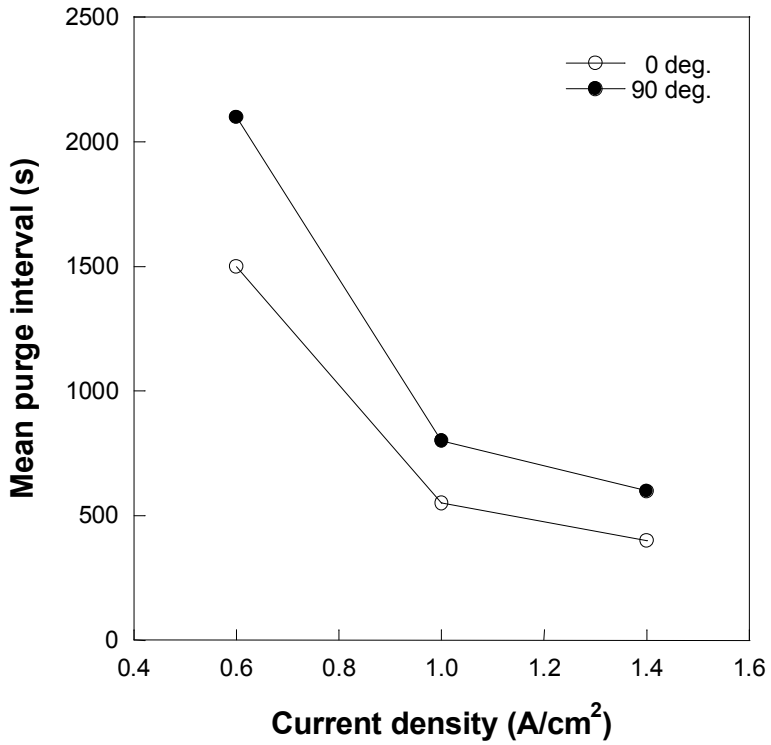


**Fig. 3.21** Variation of mean purge interval in cathodic dead-end operation.

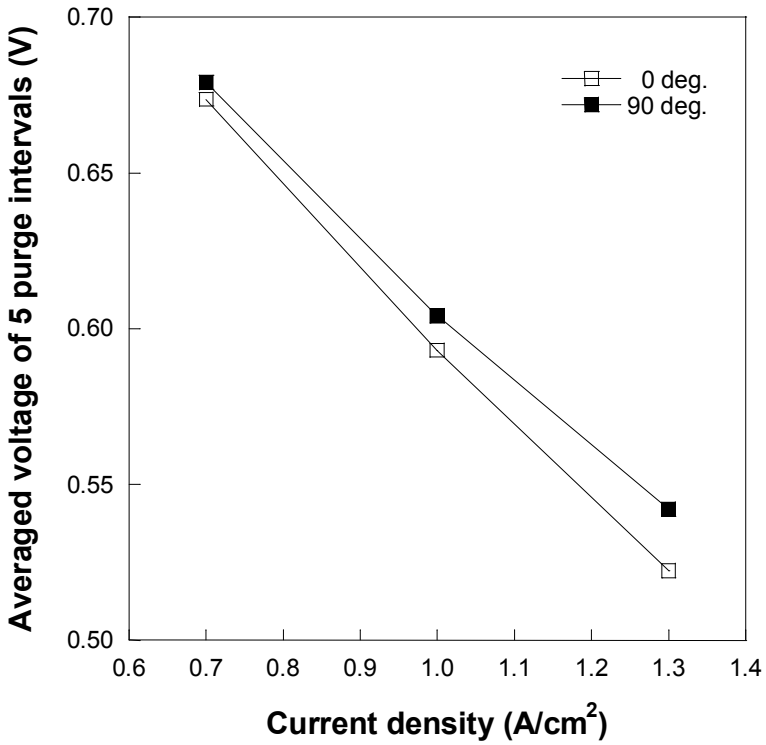


**Fig. 3.22** Variation of averaged voltage of 5 purge intervals in cathodic dead-end operation.

## 3.4 Summary

In this chapter, we investigated the effect of GDL anisotropic characteristics on performance of open mode fuel cell and purge characteristics of dead-end mode fuel cell. Fuel cells with 90° GDLs, whose directions of higher stiffness is perpendicular to the major flow and 0° GDLs, whose directions of higher stiffness is parallel to the major flow were prepared.

In open mode, experimental studies were conducted to elucidate the correlation between anisotropic bending stiffness of a GDL and geometry of bipolar plates such as land/channel width ratio and channel depth. BP-1, 2 and 3 which have land/channel width ratios of 0.27, 0.75 and 1.12, respectively at same channel depth were prepared. Also, BP-4, 5 and 6 which have channel depths of 0.2, 0.6 and 1.0, respectively at same land/channel width ratio were prepared. I-V performances of fuel cell with the 90° GDL were higher than those of fuel cell with the 0° GDL in all BPs due to the higher resistance of 90° GDL to cell assembly. As the land/channel width ratio increased, the difference of the I-V performances of the fuel cells with both the 90° and 0° GDLs decreased due to sufficient supporting of the wider land. In high current density, the voltage of BP-2 is higher than the BP-1 and 3 meaning that there are two competing factors of contact resistance and pressure difference. The

voltage of the BP-4 is the lowest and the difference of the BP-5 and 6 was negligible. The difference of the BP-4 was lower than the BP-5 and 6 implying that effect of anisotropic bending stiffness of the GDLs increase till specific point, but not over the point. Above I-V performance results were supported by HFR and pressure difference. The HFR differences between the fuel cells with the 90° and 0° GDLs of BP-1 were higher than BP-2 indicating that the effects of anisotropic bending stiffness of GDL on the deformations is highest at low land/channel width ratio. Also, the HFR values of both 90° and 0° GDL cells with BP-4 were higher than those of cells with BP-5, 6 as shown in Fig 3.9. The results indicate that shallow channel volume of the BP-4 may induce the higher pressure in gas channel and thus contact status at the interfaces between the GDLs and land may also deteriorated. The difference of air $\Delta P$ between fuel cells with BP-4 has significantly higher than cells with the BP-5 and 6 having almost no $\Delta P$.

In dead-end mode, the peak voltage of the 0° GDL cell was also higher than 90° GDL indicating the higher contact resistance in 0° GDL cell. Also, the purge interval of the fuel cell with 0° GDL was also longer than that of the fuel cell with 90° GDL implying the difference of GDL porosity reduction between both to 90° and 0° GDL cells at same cell assembly pressure. The averaged voltages of 90° GDL cell were higher than those of 0° GDL cell and

the difference is more obvious at higher current density owing to the higher contact resistance in the higher current density.

# Chapter 4. Theoretical analysis on GDL anisotropic characteristics

## 4.1 Introduction

In chapter 3, we identified that clamping pressure for sealing fuel cell components changes the GDL thickness affecting contact resistance and pressure difference. This change of thickness affects GDL material characteristics such as heat conductivity, electric conductivity, porosity and gas permeability. In particular, the changes of the gas permeability significantly influence on mass transport in GDL affecting the cell performance. The clamping pressure affects gas permeability of GDL. So, Studies about the GDL have been conducted experimentally [44-46] and numerically [47-50]. However, studies about gas permeability of GDL in-plane anisotropy were quite rare. It can be easily estimated that the gas permeability of GDL can be appeared differently at 90° and 0° GDLs after cell assembly because of the difference of deformation. Furthermore, it was identified that the clamping pressure leads to different porosities between 90° and 0° GDLs. The different porosities of 90° and 0° GDLs after cell assembly can influence on the fuel cell performance. To clarify the difference effects of anisotropic GDLs on cell performance, numerical studies using Computational fluid dynamics (CFD) were conducted in this study.

## 4.2 Experiment for measuring the GDL permeability

In this study, permeability of the anisotropic GDL samples as a function of GDL porosity was measured. The porosity of the compressed GDL can be obtained from the original GDL and gasket thickness as follows [51]:

$$CR = \frac{\delta_{GDL} - \delta_{pressed}}{\delta_{GDL}} \tag{4.2}$$

Where $\delta_{GDL}$ and $\delta_{pressed}$ are original and pressed GDL's thickness, respectively. Cross-sectional view of GDL after compression for assembling the cell components was represented as shown in Fig 4.1. Then, the GDL porosity of the compressed GDL can be obtained as follows [52]:

$$\varepsilon_c = \frac{\varepsilon - CR}{1 - CR} \tag{4.3}$$

where $\varepsilon$ and $\varepsilon_c$ are the original GDL and compressed GDL's porosity, respectively. The thickness variation of anisotropic GDLs used for this study referred to the thickness values of anisotropic GDLs measured according to compression in the literature [16].

### 4.2.1 Experimental setup

In this section, experimental apparatus and setups for measuring the through and in-plane permeability are represented. Mass flow through a porous medium is described by Darcy's Law [53] as follow:

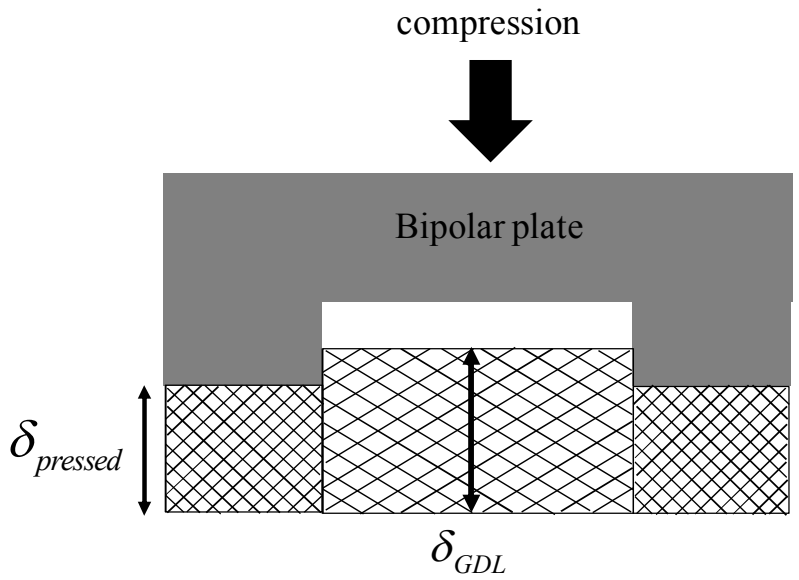


**Fig. 4. 1** Cross-sectional view of GDL after compression.

$$-\nabla P = \frac{\mu}{K} v \tag{4.3}$$

where K is the gas permeability of the porous material, P the pressure, $v$ the superficial velocity, μ is the viscosity of the flowing fluid. Many studies for measuring permeability of the GDL were conducted [49, 54-56]. They obtained the gas permeability by measurement of only pressure differences at the Darcy's Law because the viscosity of fluid is constant and the velocity of GDL is also constant at fixed flow rate. We followed the above method for obtaining the gas permeability. But, we need to measure the thickness and permeability at the same time. Thus, the apparatus was contrived as shown in Fig. 4.2. In-plane and through-plane gas permeability can be measured by change of flow direction at this apparatus. Fig. 4.3 shows cross-sectional diagram of experimental apparatus for measuring in-plane (a) and through-plane (b) gas permeability. The sample size for test of in-plane permeability was 20mm × 10 mm and that of through-plane was 10mm × 10 mm.

Thickness variations of the samples were measured using Mitutoyo depth micrometer. Fig. 4.4 shows force measurement system for applying the compression force. A Push-Pull guage (SKN-5, SUNDOO, China) that can measure forces of up to 5000N was used to apply the compression force. Depth micrometer for measuring the GDL thickness is located between the bottom surface of force measurement system and top surface of bar applying compression force. Measurements for at least 10 GDL thicknesses were obtained at other locations and measurements for at least 10 flow rates were

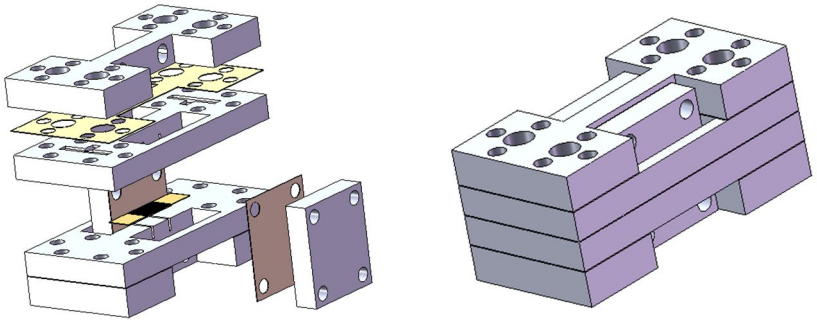

**(a) solid figure of apparatus**

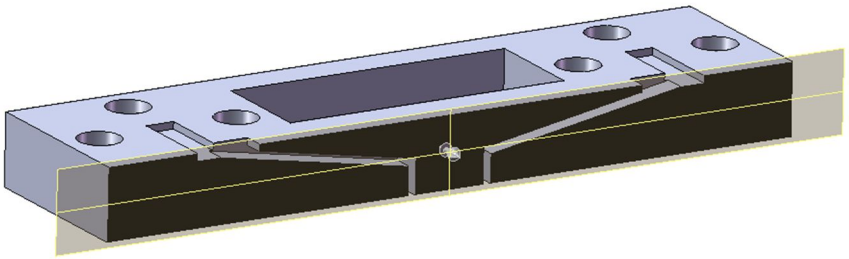

**(b) cross-sectional figure**

**Fig. 4. 2** Experimental apparatus for permeability measurement.

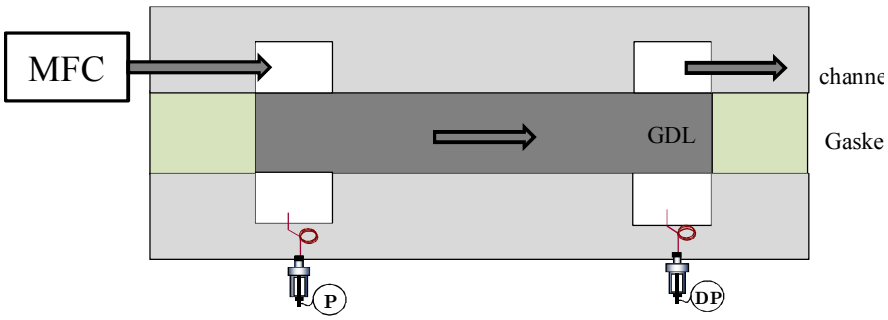


**(a) In-plane**

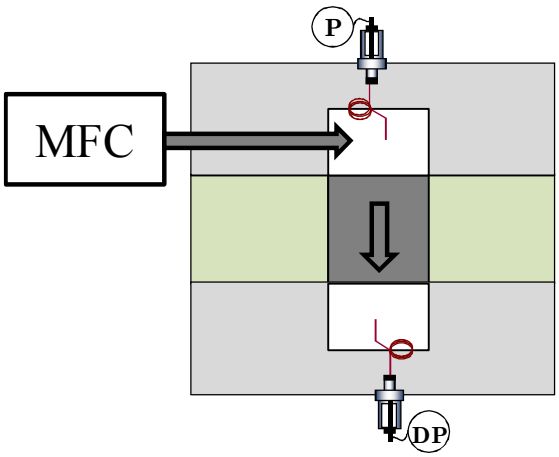


**(b) Through-plane**

**Fig. 4. 3** Cross-sectional diagram of experimental apparatus for measuring in and through-plane permeability.

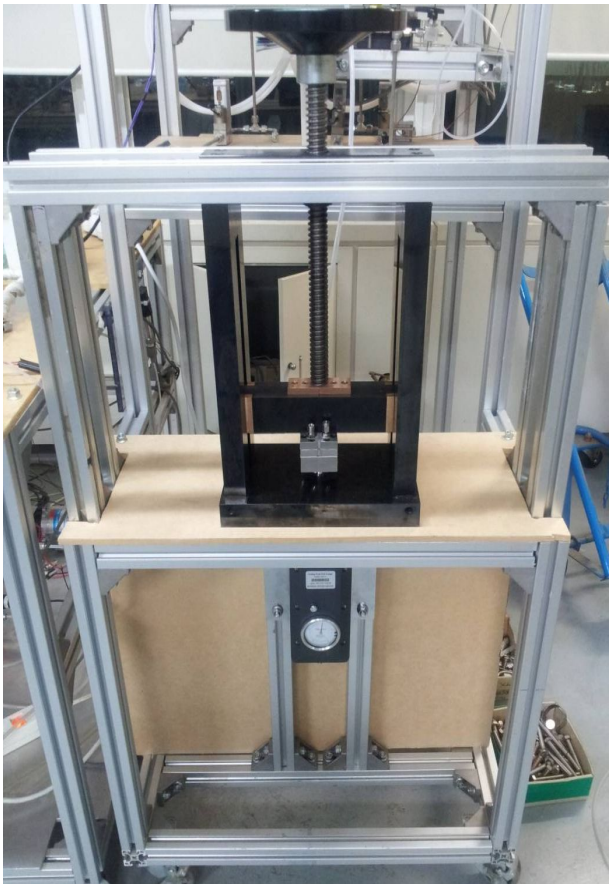

**Fig. 4. 4** Force measurement system for applying the compression force.

obtained at each GDL thickness. A leakage test was performed to check the sealing condition after the apparatus components were assembled. Instruments for measuring gas pressure and mass flow rate are same as those used in chapter 4.

### 4.2.2 Measurement of permeability

In one-dimensional flow, Eq. (4.3) is solved as follows [57]:

$$P_{in}^2 - P_{out}^2 = \frac{2RTL}{M}\frac{\mu}{K}m' \tag{4.4}$$

where $P_{in}$ is the inlet pressure, $P_{out}$ the outlet pressure, $R$ the universal gas constant, $T$ the temperature, $M$ the molecular weight of air, $m'$ the mass flux through the sample and L is the length of the sample in case of in-plane flow and the thickness of the sample in case of through-plane flow. In in-plane measurement, the machine direction of 90° GDL is parallel with flow direction and that of 0° GDL is perpendicular with flow direction. Fig. 4.5 shows the experimental data of in-plane pressure drop as a function of air mass flux of anisotropic GDL before the compression. The slope of 0° GDL was $4.27\times e^{10}$, which has higher value than that of 90° GDL having the value of $2.78\times e^{10}$, implying the lower permeability of 0° GDL. Also, this result indicates that the permeability of the machine direction of GDL is higher than that of cross-machine direction. The slope of the experimental data of through-plane pressure drop is $3.78\times e^{10}$ as shown in Fig. 4.6, which have the value between 90° and 0° GDL in in-plane pressure drop data. Fig. 4.7

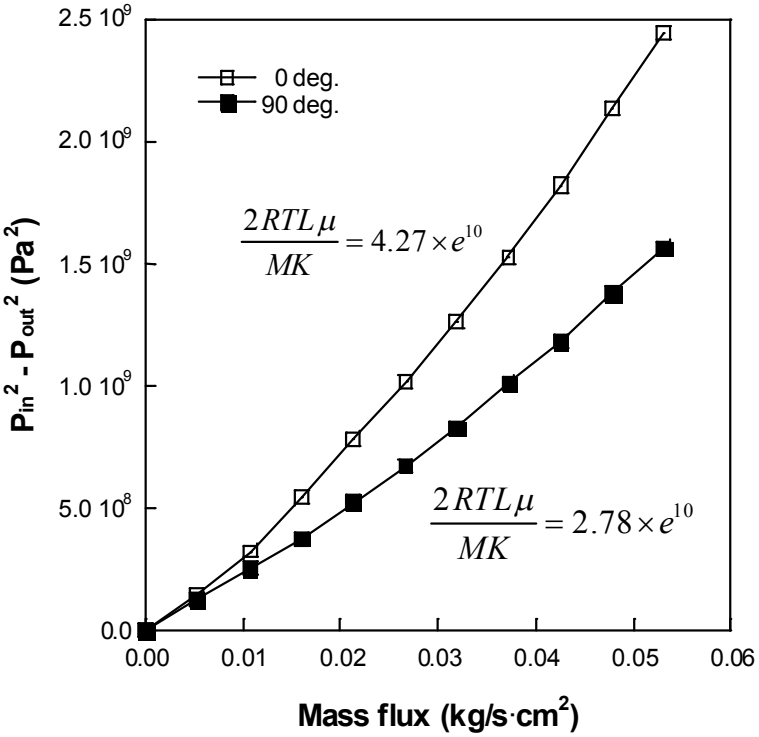


**Fig. 4. 5** Experimental data of in-plane pressure drop as a function of air mass flux of anisotropic GDL before the compression.

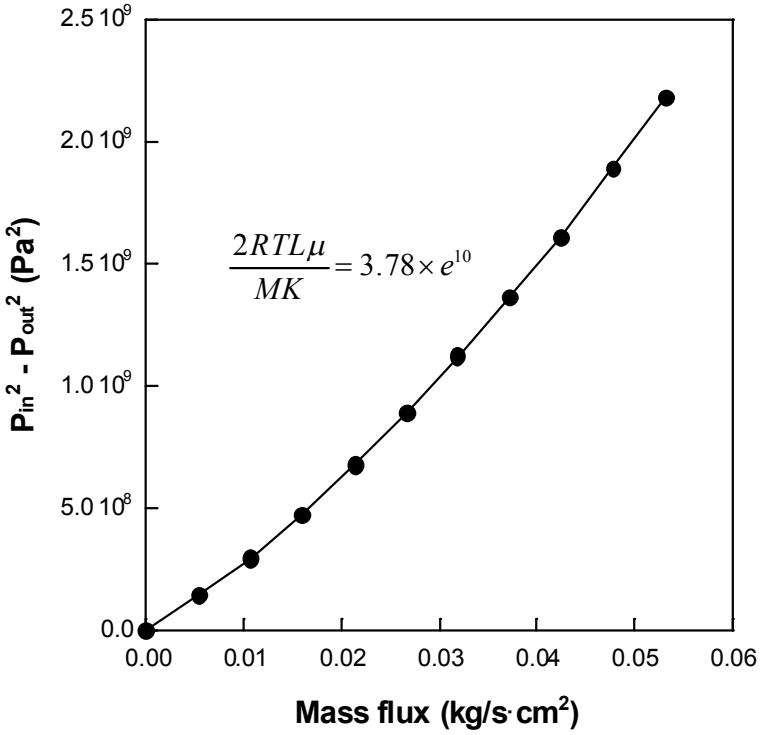


**Fig. 4. 6** Experimental data of through-plane pressure drop as a function of air mass flux of anisotropic GDL before the compression.

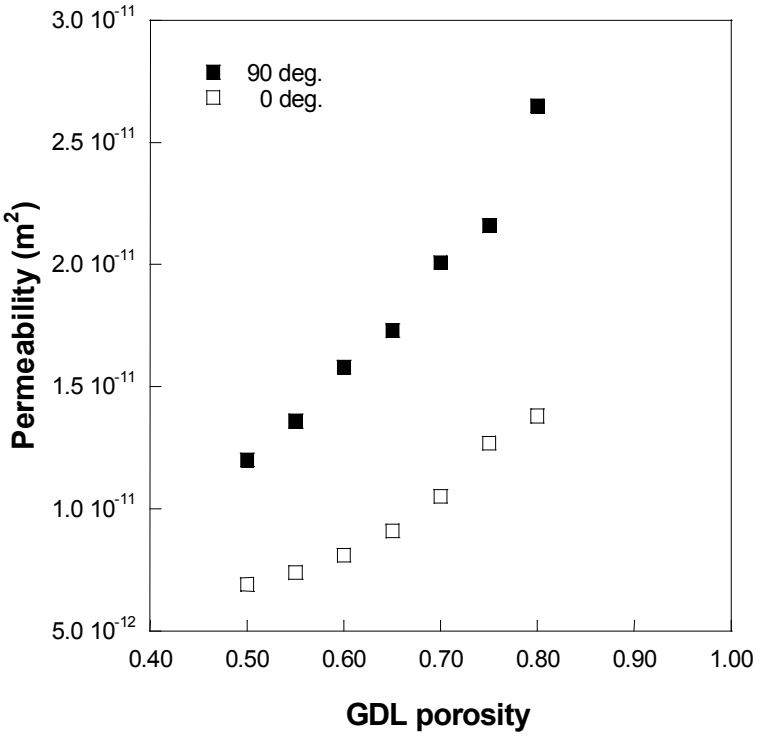


**Fig. 4. 7** In-plane permeability as a function of anisotropic GDL's porosity after the compression.

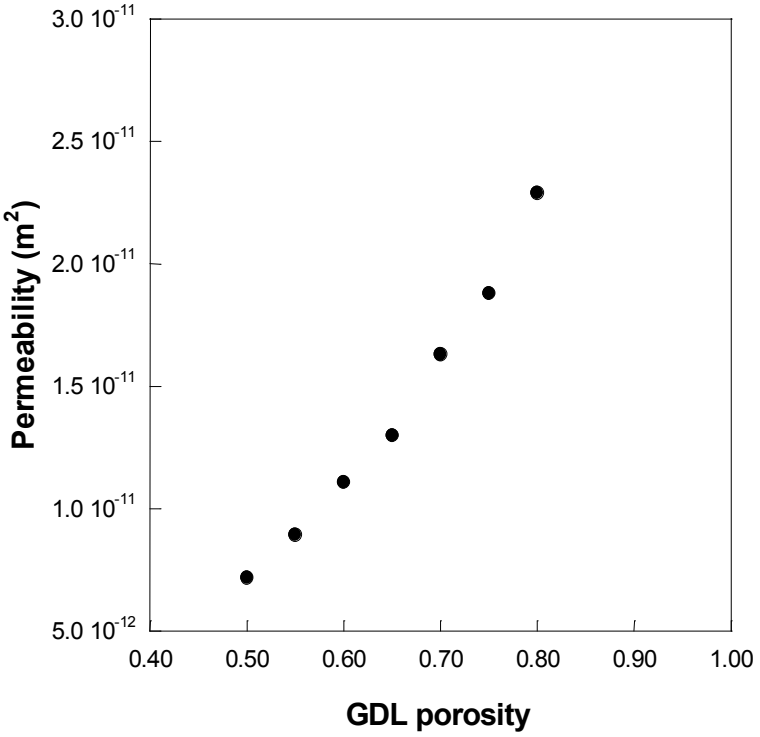


**Fig. 4. 8** Through-plane permeability as a function of anisotropic GDL's porosity after the compression

.

shows the In-plane permeability as a function of GDL porosity after the compression. The permeability of anisotropic GDLs exponentially increased according to increase of the GDL porosity. The trend was similar with the results in Ref. [56]. The permeability of the 90° GDL was higher than that of 0° GDL in all porosities. It can estimated by this result that the 90° GDL can lead to higher channel to channel crossover than the 0° GDL. The through-plane permeability values as a function of GDL porosity were distributed between the in-plane permeability values of 90° and 0° GDLs as shown in Fig. 4.8, which the trend is similar with Fig 4.6.

## 4.3 Mesh generation and model conditions

For clarifying the effects of anisotropic GDLs on flow characteristics of single fuel cell, CFD program based on STAR-CD version 4.16, a commercial finite volume technique solver was used. The fully coupled governing equations were solved by this software with add-on tool called ES-PEM version 2.50.

### 4.3.1 Model assumptions

The specific assumptions of this numerical study are as follows [58]:

(1) The gas is ideal gas.

(2) All the gas and water fractions is characterized by mixture transport

(3) Water in channel exists as very tiny droplets.

(4) Incompressible and laminar flow due to a small pressure gradient and low flow velocities.

(5) Effect of immobile liquid saturation in the porous diffusion medium is negligible.

(6) Liquid film is formed on the electrode surface during liquid water condensation.

(7) Liquid water is in the form of small droplets and freely suspended in the gas flow.

Also, properties and parameters for CFD modeling and operating conditions used in this study are presented in Table 4.1 and 4.2, respectively.

### 4.3.2 Governing equations

The overall cell voltage considering the activation loss and the ohmic loss can be expressed by Eq. 4.5

$$V_{cell} = V_{OCV} - \eta(x,y) - IR(x,y) \tag{4.5}$$

$$\begin{aligned}\eta(x,y) &= \eta_C + \eta_A \\ &= \frac{RT(x,y,anGDL/MEA)}{\alpha_c F}\ln\left[\frac{I(x,y)P(x,y,caGDL/MEA)}{I_{O,C}P_{O_2}(x,y,caGDL/MEA)}\right] \\ &+ \frac{RT(x,y,anGDL/MEA)}{\alpha_a F}\ln\left[\frac{I(x,y)P(x,y,anGDL/MEA)}{I_{O,A}P_{H_2}(x,y,anGDL/MEA)}\right]\end{aligned} \tag{4.6}$$

**Table 4.1** Properties of fuel cell components for CFD modeling.

| Parameter | | unit | Inlet conditions (an/ca) |
|---|---|---|---|
| Channel | Height | mm | |
| Bipolar plate | Channel | mm | 65 |
| | Land | mm | |
| GDL | Thickness | $\mu$m | 278 |
| | Thermal conductivity | W/m·K | 0.21 |
| | Porosity before compression | - | 0.78 |
| MEA | thickness | $M$m | 25.4 |
| | Thermal conductivity | W/m·K | 0.15 |
| | Transfer coefficient (Cathode/Anode) | - | 0.6 / 0.2 |
| | Exchange current density (Cathode/Anode) | A/cm$^2$ | 0.02 / 0.2 |

**Table 4.2** Operating conditions used in this study.

| Parameter | | unit | values |
|---|---|---|---|
| Anode | Stoichiometric ratio | - | 1.5 |
| | Inlet temperature | ℃ | 65 |
| | Inlet relative humidity | % | 100 |
| | Mass fraction of hydrogen | - | 0.078 |
| | Mass fraction of water | - | 0.561 |
| Cathode | Stoichiometric ratio | - | 2.0 |
| | Inlet temperature | ℃ | 65 |
| | Inlet relative humidity | % | 100 |
| | Mass fraction of hydrogen | - | 0.169 |
| | Mass fraction of water | - | 0.274 |
| Operating conditions | Exit pressure | kPa | 101 |
| | Open circuit voltage | V | 0.96 |
| | Cell temperature | ℃ | 65 |

$$IR(x,y) = I(x,y)\frac{t_m}{\sigma_m(x,y)} \tag{4.7}$$

where $\eta_c$, $\eta_a$, IR are cathode overpotential, anode overpotential and ohmic loss, $t_m$ is membrane thickness, $\sigma_m(x,y)$ is local membrane conductivity, F is Faraday constant, $\alpha_c$ is cathode charge transfer coefficient, $\alpha_a$ is anode charge transfer coefficient, $I_{O,C}$ is cathode exchange current density, $I_{O,A}$ is cathode exchange current density, T(x,y) is local temperature and P(x,y) is local pressure.

The governing equations for model are presented in table 4.3. The transport phenomena are coupled with the equations for mass conservation, momentum transport, gas transport, water transport and Energy equation. Source terms for governing equations are presented in table 4.4. The water is generated at cathode catalyst layer due to the reaction of fuels. In this study, it was assumed that gas and water sources are generated from anode or cathode GDL/MEA interface. The permeability of GDL is applied to Eq. 4.16 showing momentum transport of GDL. The $\beta$ at Eq. 4.16 is gas permeability in GDL, and thus it is estimated at the equation that high gas permeability can reduce the momentum drop through the GDL. Also, different in-plane permeability of anisotropic GDLs can influence on channel to channel crossover flow. Table 4.5 presents mass diffusion, water transport and water film thickness. The water is transported from anode to cathode by the electro-osmotic drag. On the contrary, the water transport form cathode to anode by back diffusion due to water concentration difference. This water balance is decided by α of Eq. 4.25. When the water

activity of water exceeded 1.0, water vapor was condensed to liquid until the activity reach 1.0. Conversely, when liquid water was present and the activity dropped below 1.0, then liquid water was evaporated until the water

**Table 4.3** Governing equations.

| Parameter | Mathematical expressions | |
|---|---|---|
| Conservation of mass | $\frac{\partial(\rho u)}{\partial x}+\frac{\partial(\rho v)}{\partial y}+\frac{\partial(\rho \omega)}{\partial z}=S_m$ | (4.8) |
| Momentum transport | $u\frac{\partial(\rho u)}{\partial x}+v\frac{\partial(\rho u)}{\partial y}+w\frac{\partial(\rho u)}{\partial z}=-\frac{\partial P}{\partial x}+\frac{\partial}{\partial x}(\mu\frac{\partial u}{\partial x})+\frac{\partial}{\partial x}(\mu\frac{\partial u}{\partial y})+\frac{\partial}{\partial z}(\mu\frac{\partial u}{\partial z})+S_{px}$<br>$u\frac{\partial(\rho v)}{\partial x}+v\frac{\partial(\rho v)}{\partial y}+w\frac{\partial(\rho v)}{\partial z}=-\frac{\partial P}{\partial x}+\frac{\partial}{\partial x}(\mu\frac{\partial v}{\partial x})+\frac{\partial}{\partial x}(\mu\frac{\partial v}{\partial y})+\frac{\partial}{\partial z}(\mu\frac{\partial v}{\partial z})+S_{py}$<br>$u\frac{\partial(\rho w)}{\partial x}+v\frac{\partial(\rho w)}{\partial y}+w\frac{\partial(\rho w)}{\partial z}=-\frac{\partial P}{\partial x}+\frac{\partial}{\partial x}(\mu\frac{\partial w}{\partial x})+\frac{\partial}{\partial x}(\mu\frac{\partial w}{\partial y})+\frac{\partial}{\partial z}(\mu\frac{\partial w}{\partial z})+S_{pz}$ | (4.9) |
| Hydrogen transport | $u\frac{\partial(\rho m_{H_2})}{\partial x}+v\frac{\partial(\rho m_{H_2})}{\partial y}+w\frac{\partial(\rho m_{H_2})}{\partial z}=\frac{\partial(J_{x,H_2}m_{H_2})}{\partial x}+\frac{\partial(J_{y,H_2}m_{H_2})}{\partial y}+\frac{\partial(J_{z,H_2}m_{H_2})}{\partial z}+S_{H_2}$ | (4.10) |
| Water vapor transport | $u\frac{\partial(\rho m_{wv})}{\partial x}+v\frac{\partial(\rho m_{wv})}{\partial y}+w\frac{\partial(\rho m_{wv})}{\partial z}=\frac{\partial(J_{x,wv}m_{wv})}{\partial x}+\frac{\partial(J_{y,wv}m_{wv})}{\partial y}+\frac{\partial(J_{z,wv}m_{wv})}{\partial z}+S_{wv_p}+S_{awv_e}+S_{cwv_e}$ | (4.11) |
| Water liquid transport | $u\frac{\partial(\rho m_{wl})}{\partial x}+v\frac{\partial(\rho m_{wl})}{\partial y}+w\frac{\partial(\rho m_{wl})}{\partial z}=\frac{\partial(J_{x,wl}m_{wl})}{\partial x}+\frac{\partial(J_{y,wl}m_{wl})}{\partial y}+\frac{\partial(J_{z,wl}m_{wl})}{\partial z}+S_{wl_p}$ | (4.12) |
| Oxygen transport | $u\frac{\partial(\rho m_{O_2})}{\partial x}+v\frac{\partial(\rho m_{O_2})}{\partial y}+w\frac{\partial(\rho m_{O_2})}{\partial z}=\frac{\partial(J_{x,O_2}m_{O_2})}{\partial x}+\frac{\partial(J_{y,O_2}m_{O_2})}{\partial y}+\frac{\partial(J_{z,O_2}m_{O_2})}{\partial z}+S_{O_2}$ | (4.13) |
| Energy equation | $\frac{\partial(\rho uh)}{\partial x}+\frac{\partial(\rho vh)}{\partial y}+\frac{\partial(\rho wh)}{\partial z}=\frac{\partial}{\partial x}\left(k\frac{\partial T}{\partial x}\right)+\frac{\partial}{\partial y}\left(k\frac{\partial T}{\partial y}\right)+\frac{\partial}{\partial z}\left(k\frac{\partial T}{\partial z}\right)+S_{h_p}+S_{h_e}$ | (4.14) |

**Table 4.4** Source terms for governing equations

| Parameter | Mathematical expressions | | |
|---|---|---|---|
| Conservation of mass | $S_m = S_{H_2} + S_{wv_p} + S_{wl_p} + S_{awv_e}$ | at anode GDL/MEA interface | (4.15) |
| | $S_m = S_{O_2} + S_{wv_p} + S_{wl_p} + S_{cwv_e}$ | at cathode GDL/MEA interface | |
| Momentum transport | $S_{px} = -\frac{\mu u}{\beta_x} \qquad S_{py} = -\frac{\mu v}{\beta_y} \qquad S_{pz} = -\frac{\mu w}{\beta_z}$ | at GDL | (4.16) |
| Hydrogen transport | $S_{H_2} = -\frac{I(x,y)}{2F} M_{H_2} A_{cv}$ | at anode GDL/MEA interface | (4.17) |
| Water vapor transport | $S_{wv_p} = \frac{M_{H_2O} \sum \frac{mass_n \, of \, v}{M_n \, of \, v}}{\left(1 - \frac{P_{wv}^{sat}}{P}\right)} \left[\frac{P_{wv}^{sat} - P_{wv}}{P}\right] \times r$ | at entire fluid domain | (4.18) |
| | $S_{awv_e} = -\frac{\alpha(x,y)}{F} I(x,y) M_{H_2O} A_{cv}$ | at anode GDL/MEA interface | (4.19) |
| | $S_{cwv_e} = -\frac{1+2\alpha(x,y)}{2F} I(x,y) M_{H_2O} A_{cv}$ | at cathode GDL/MEA interface | (4.20) |
| Water liquid transport | $S_{wl_p} = -S_{wv_p}$ | at entire fluid domain | (4.21) |
| Oxygen transport | $S_{O_2} = -\frac{I(x,y)}{4F} M_{O_2} A_{cv}$ | at cathode GDL/MEA interface | (4.22) |
| Energy equation | $S_{h_e} = h_{rxn} \times \left[\frac{1}{2F} I(x,y) \times A_{cv}\right] - (I(x,y) V_{cell} A_{cv})$ | at cathode GDL/MEA interface | (4.23) |

**Table 4.5** Constitutive equations for modeling electrochemical effects

| Parameter | Mathematical expressions | |
|---|---|---|
| Diffusion mass flux of species n in ξ direction | $J_{\xi,n} = -\rho D_{\xi,n} \frac{\partial m_{K,n}}{\partial \xi}$ | (4.24) |
| Net water transfer coefficient per proton | $\alpha(x,y) = n_d(x,y) - \frac{F}{I(x,y)} D_w(x,y) \frac{(C_{wc}(x,y) - C_{wa}(x,y))}{t_m}$ | (4.25) |
| Water content in the membrane | $\lambda = 0.043 + 17.81 a_m - 39.85 a_m^2 + 36.0 a_m^3 \ \ (0 < a_m \le 1)$<br>$= 14 + 1.4(a_a - 1) \ \ (1 < a_m \le 3)$ | (4.26) |
| Water diffusion coefficient | $D_w = D_\lambda \exp(2416(\frac{1}{303} - \frac{1}{T(x,y)}))$ | (4.27) |
| Water vapor concentration for anode and cathode surfaces of the MEA | $C_{wK}(x,y) = \frac{\rho_{m,dry}}{M_{m,dry}}(0.043 + 17.8 a_K - 39.8 a_K^2 + 36.0 a_K^3) \quad (a_K \le 1)$<br>$= \frac{\rho_{m,dry}}{M_{m,dry}}(14 + 1.4(a_K - 1)) \quad (a_K > 1)$ | (4.28) |
| Water activity | $a_K = \frac{X_{w,K} P(x,y)}{P_{w,K}^{sat}}$ | (4.29) |
| Water film thickness | $t_{f,k} = \frac{m_{w,l(\sum mass_n)}}{\varepsilon \rho_{wl} Area_{cv}}$ | (4.30) |
| Gas solubility | $-\frac{I(x,y)}{4F} M_{O_2} = \rho m_{O_2} D_{O_2,l} \left[ \frac{X_{O_2}(x,t,z - t_{f,c}) P(x,y,z - t_{f,c}) H_{O_2,l}^{-1} - X_{O_2}(x,y,z)}{t_{f,c}} \right]$<br>$-\frac{I(x,y)}{2F} M_{H_2} = \rho m_{H_2} D_{H_2,l} \left[ \frac{X_{H_2}(x,t,z - t_{f,a}) P(x,y,z - t_{f,a}) H_{H_2,l}^{-1} - X_{H_2}(x,y,z)}{t_{f,a}} \right]$ | (4.31) |

activity reach to 1.0. When liquid water condensed in the region adjacent to the electrode surface, liquid film is formed on the electrode surface. Hydrogen and oxygen were required to dissolve in the liquid film and diffuse through the film to the electrode surface in order to react. Henry's law was used to calculate the solubility of the gases in the liquid. The thickness of liquid film depends on the condensation rate.

Fig. 4.9 shows schematic illustration of the channel geometry for modeling the effects of anisotropic GDL. 25 $cm^2$ serpentine flow-fields of 4-turns were considered in this study. For analyzing characteristics of anisotropic GDL, the permeability of different direction was set in CFD tool. For instance, higher permeability of in-plane directions was applied to 90° direction at Fig. 4.9 and lower permeability was applied to 0° direction. Furthermore, reduced thickness and permeability by compression were considered. Fig. 4.10 shows the schematic illustration of a computational domain to model the effects of anisotropic GDLs. In practice, the permeability of GDL under channel and land is different. Therefore, we composed the cell mesh structures differently under channel and land. The GDL properties (permeability and porosity) before compression were applied at the deep blue section in Fig. 4.10 and conversely, the GDL properties after compression were applied at the light blue section in Fig. 4.10. Also, GDL properties were applied differently according to compressed thickness.

The uniform grid cells are established and the SIMPLE algorithm was applied with an algebraic multi-grid method for the solution procedure to

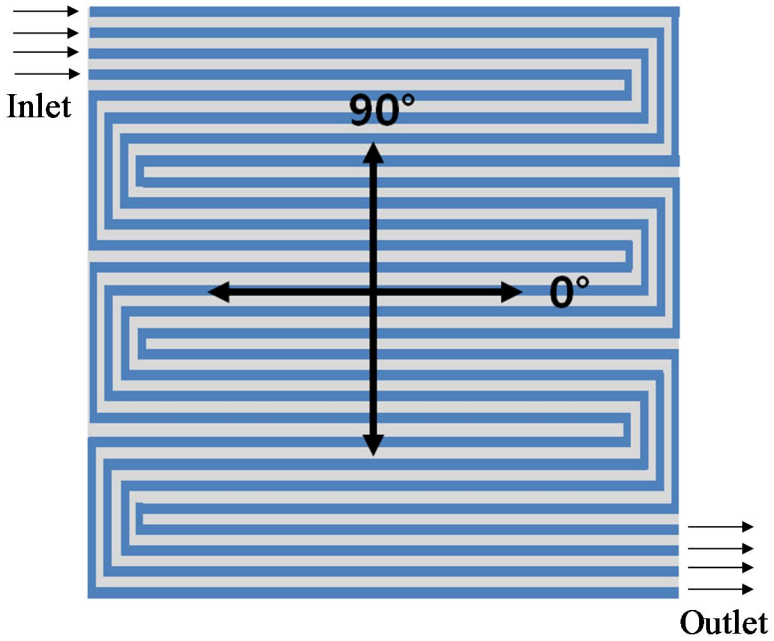


**Fig. 4. 9** Channel geometry of a computational domain to model the effects of anisotropic GDLs.

.

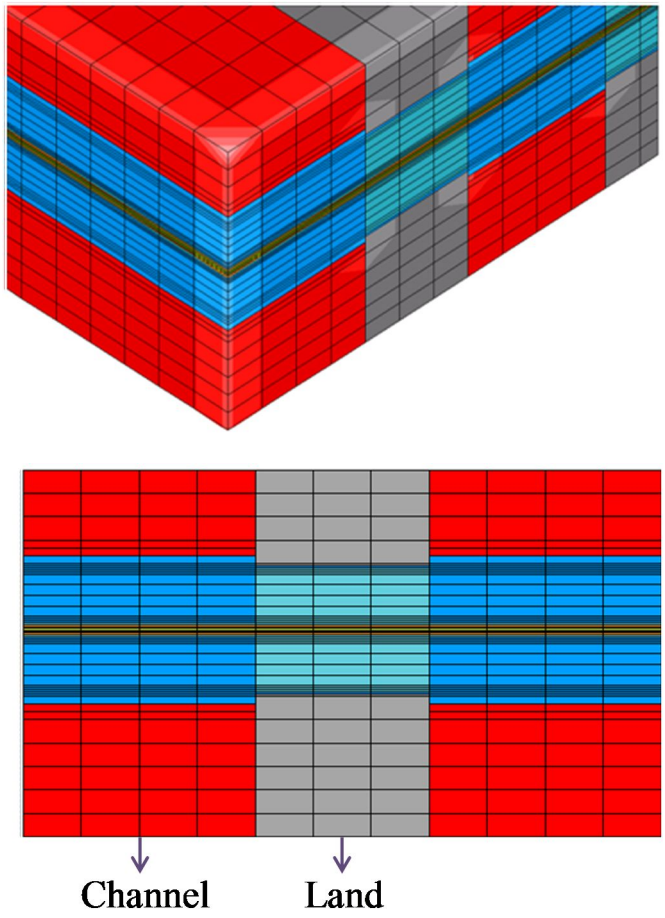


**Fig. 4.10** Schematic illustration of mesh generation to model the effects of anisotropic GDLs.

.

solve flow-field. The properties and parameter taken from Ref. [59] are given in Table 4.1. Operating conditions including inlet conditions, cell temperature and exit pressure used in this study.

## 4.4 Results and discussion

In this chapter, the effects of gas permeations through the cell channels between fuel cells with 90° and 0° GDLs on the difference of performances was investigated numerically. Current density distribution at cathode MEA and gas velocity in cathode GDL are simulated. Fig. 4.11 and 4.12 present the current density distributions at cathode MEA at 0.9 A.cm$^2$. In the overall distribution, the local current of inlet was higher that of outlet because of higher oxygen concentration. The local current density becomes lower toward the outlet of channel by reaction of oxygen. More noteworthy is that current density distribution of fuel cell with 90° GDL was relatively more uniform than that with 0° GDL, indicating that oxygen in GDL distributed more uniformly. Also, current density of 90° GDL cell at 1.5 A/cm$^2$ was distributed in reaction area more uniformly than that of 0.9 A/cm$^2$. The results indicate that higher flow rate lead to more gas permeation through the cell channels. By this effect, the voltage value of 90° GDL cell was higher than that of 0° GDL cell in overall current density conditions. The voltage values of the two GDL cells at current density of 0.9 A/cm$^2$ are 0.592 and 0.598 V, respectively, showing no significant difference. However, the voltage values of the two GDL cells at current density of 0.9 A/cm$^2$ are

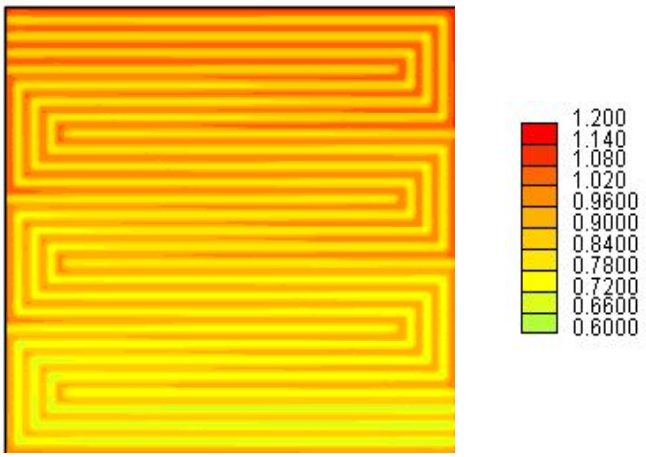


**(a) 0° GDL cell (0.592 V)**

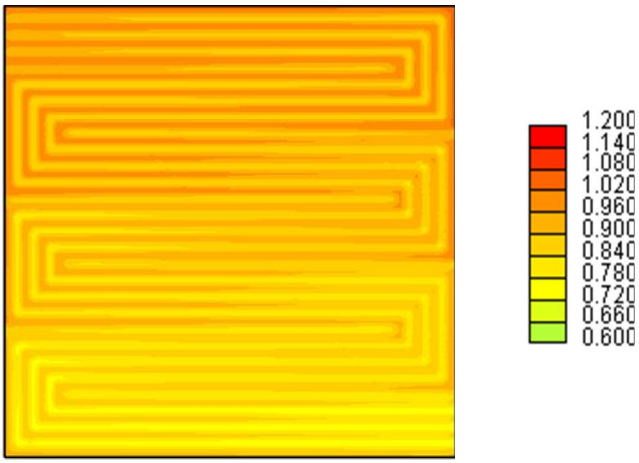


**(b) 90° GDL cell (0.598 V)**

**Fig. 4.11** Current density distributions at cathode MEA at 0.9 A/cm$^2$.

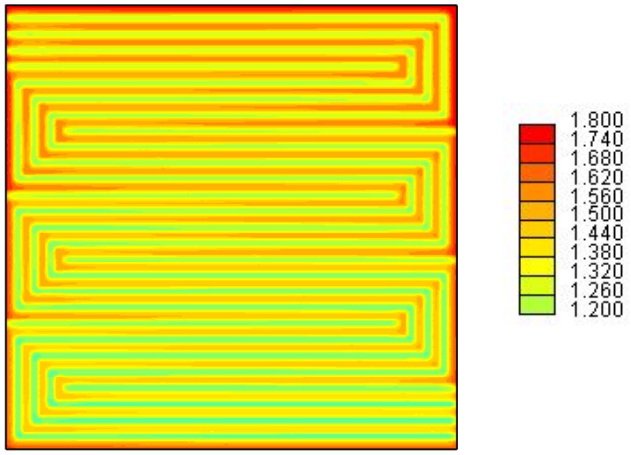


**(a) 0° GDL cell (0.368 V)**

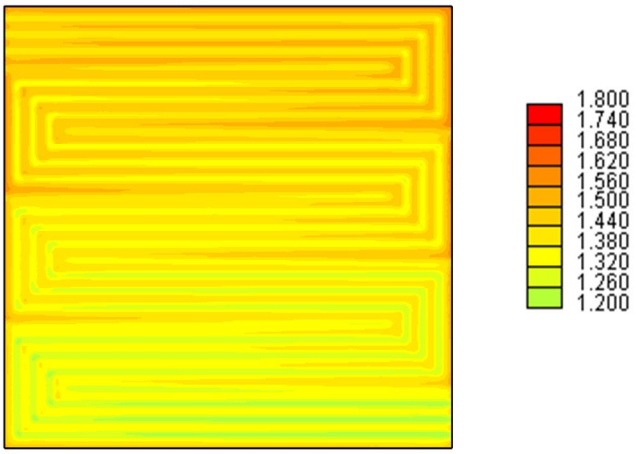


**(b) 90° GDL cell (0.391 V)**

**Fig. 4.12** Current density distributions at cathode MEA at 1.5 A/cm$^2$.

0.368 and 0.391 V, respectively. The difference rate is significant value of 6.25 % compared with 1.01% of 0.9 A/cm$^2$. Fig. 4.13 shows the velocity vectors at same location in cathode GDL at 1.5 A/cm$^2$. The velocity of 90° GDL cell was higher than that of 0° GDL cell. The maximum velocity under land of 90° GDL cell was 0.5247 $e^{-1}$ m/s and about 1.74 times higher than 0.3008 $e^{-1}$ m/s of 0° GDL cell. This result can support the results about current density distribution in Fig. 4.11 and 12. I-V performance of fuel cells with anisotropic GDLs is shown in Fig. 4.14. The voltage difference in high current density over 0.9 A/cm$^2$ was relatively distinct, whereas the voltage difference in low current density below 0.9 A/cm$^2$ was negligible.

## 4.5 Summary

Numerical model using commercial computational fluid dynamics (CFD) was conducted for analyzing the effect of anisotropic GDLs on cell performance by gas permeation through the cell channel. Permeability of anisotropic GDLs for applying to model simulation was measured. Afterwards, same geometry as single cell used in chapter 3 was applied in this model. The voltage difference in high current density over 0.9 A/cm$^2$ was relatively distinct, whereas the voltage difference in low current density below 0.9 A/cm$^2$ was negligible. The simulation results show that the higher performance was induced by gas permeation through the cell channels. By

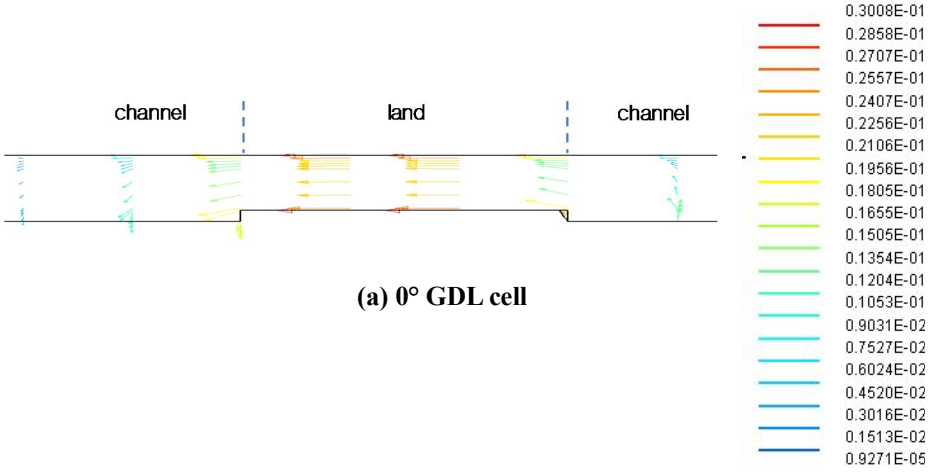


**(a) 0° GDL cell**

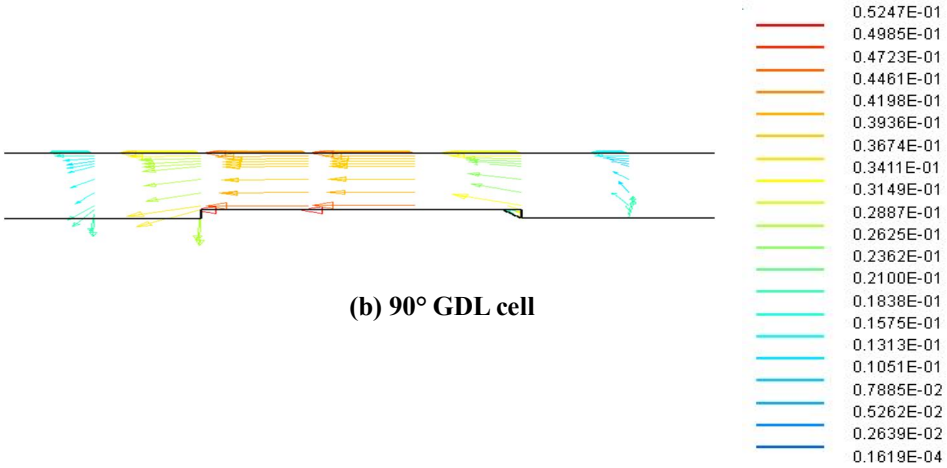


**(b) 90° GDL cell**

**Fig. 4.13** Velocity vectors in cathode GDL at 1.5 A/cm$^2$

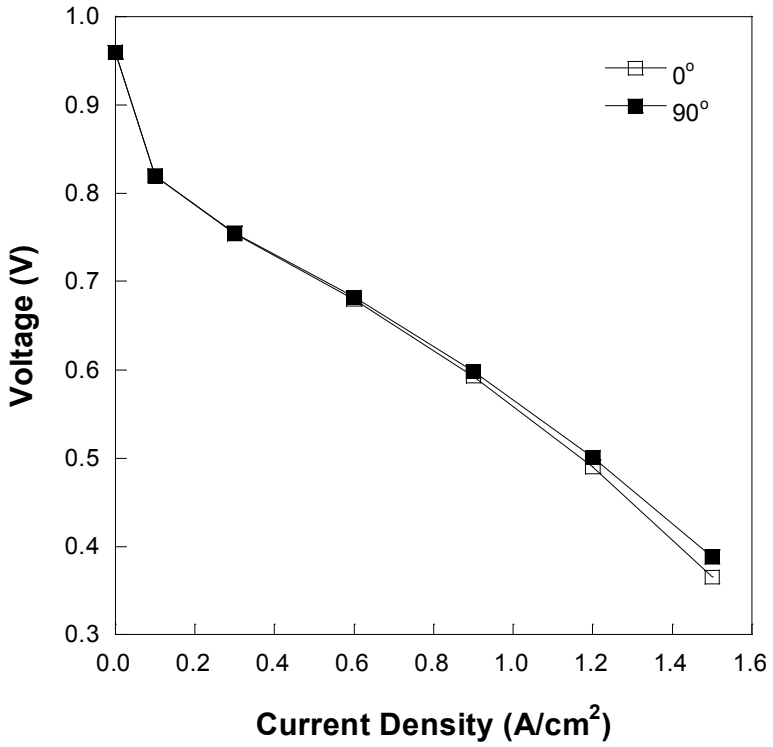


**Fig. 4.14** I-V performances of fuel cells with anisotropic GDLs.

the result, it is identified that not only contact resistance by GDL deformation but also gas permeation through the cell channel influence on the cell performance.

# Chapter 5. Effects of GDL anisotropy on fuel cell degradation

## 5.1 Introduction

Although steady-state lifetime tests can be applied to durability studies, these tests require a very long time and high costs. Therefore, accelerated stress tests (ASTs) have been widely suggested for lifetime evaluation or degradation mode analysis. Because automotive PEMFCs have dynamic operating characteristics, they experience relative humidity (RH) variations very frequently. The Repetitive RH variation induces frequent swelling/shrinkage of the membrane resulting in high mechanical stresses in MEA [13-14]. As AST to simulate the repetitive swelling/shrinking of membrane, the wet/dry cycle method of repetitively supplying wet and dry gas to fuel cell has been used. Fig. 5.1 shows a schematic diagram of the cross section of a fuel cell displaying membrane swelling and GDL intrusion into gas channels. When the fuel cell is compressed by assembly pressure, the unsupported portion of the GDL in the channel regions may intrude into the gas channels. When the membrane swells, it can impose compression to the GDL. In the present study, we focused on the deformation induced by

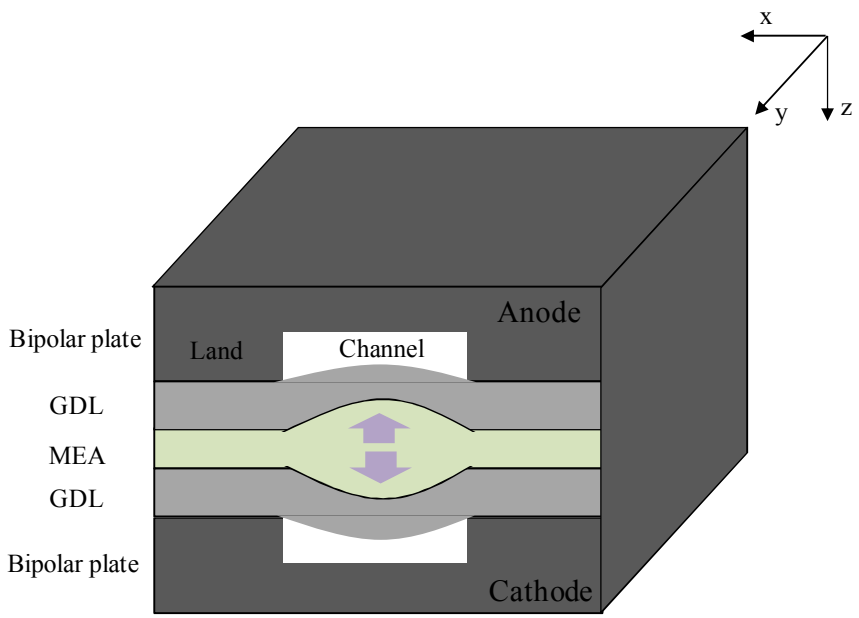


**Fig. 5. 1** Schematic diagram of cross-sectional fuel cell showing membrane swelling and GDL intrusion into gas channel.

repetitive membrane swelling caused membrane by wet/dry cycles between the MEA and GDL. The higher resistance of the 90° GDL to cell clamping compression was assumed to prevent MEA deformation by frequent swelling/shrinkage of membrane. Therefore, the degradation rates of the MEA using 90° GDL cells may be lower than that using 0° GDL cells. We prepared two representative single cells consisting of 0° and 90° GDLs and then analyzed the effects of GDL in-plane anisotropy on the mechanical degradation of the MEA. We conducted an AST to examine the mechanical durability of the MEA against repetitive supply of wet/dry gas to the fuel cell.

## 5.2 Accelerated stresses test method

### 5.2.1 Experimental setup

In this study, the fuel cell startup and shutdown were simulated by the repetitive supply of wet/dry gas. The experimental setup is shown in Fig. 5.2. The same mass flow controllers, Bubbler-type humidifiers, T-type thermocouples (TC) and Pressure transducers as chapter 2 were used. Check valves were used to provide the wet or dry gases to the fuel cell without affecting each other. Temperature control of fuel supply line, single fuel cell and bubbler humidifier is also same as chapter 2. A mass spectrometer was connected to the cathode side channel to measure the hydrogen crossover

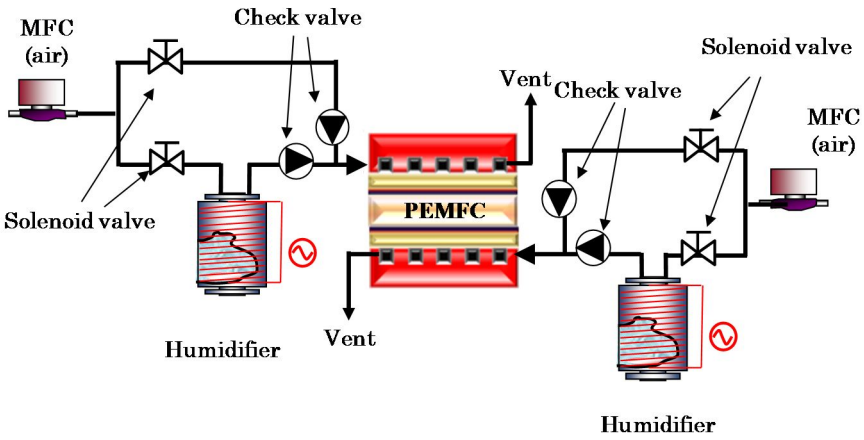


**Fig. 5. 2** Schematic diagram of experimental system for wet/dry cycles.

rate. The fuel cell was flushed for at least 1 h with a supply of pure nitrogen to measure the small amount of hydrogen correctly. An activation process was conducted before the experiments for 10 h to activate the fresh fuel cell at a cell temperature of 65°C, ambient pressure, RH of 100%/100% and stoichiometric of 1.5 and 2.0 for the anode and cathode sides, respectively. All data from the electronic equipment and sensors were transmitted to a personal computer.

### 5.2.2 Accelerated stress test method

Repetitive wet/dry cycling was conducted as an accelerated stress test method for simulating the startup and shutdown of a fuel cell. The RH of the supplied reactants was adjusted by controlling the temperature of the bubbler humidifier. As wet air that passed through the bubbler humidifier was supplied to the fuel cell inlet, the membrane absorbed the water, and the swelled membrane pushed the GDL. Conversely, when dry air that did not pass through the bubbler humidifier was supplied to the fuel cell inlet, water in the membrane evaporated and was carried out with dry air. Consequently, the membrane shrank, and the gap between the MEA and GDL widened. To simulate the repetitive swelling/shrinkage cycles automatically, the wet/dry gas was supplied selectively by solenoid valves operated by Lab-View. Dry air with 0% RH and wet air at the dew point of 85°C were supplied to the

fuel cell at a the flow rate of 2 LPM. The dew point of wet gas was maintained at 85°C by the water temperatures of the bubbler-type humidifiers. The cell and supplying gas temperatures were maintained at 80°C. Dry and wet gases were supplied into the cell for 15 and 3 min, respectively; the MEA drying process typically takes more time than the wetting process because of the highly porous structure [40]. The operating conditions and methods presented above were equally applied to both of the anode and cathode inlet gases. Experiments were conducted for up to 3000 cycles, and polarization curves and HFRs were measured every 500 cycles to analyze the cell performance and MEA durability. Hydrogen crossover rates were measured every 1000 cycles to identify the mechanical degradation or failure of the membrane. After every 500 cycles, an activation process was conducted until no more increase in performance was detected at a cell temperature of 65°C, ambient pressure, RH of 100%/100%, and stoichiometric ratios for the anode and cathode sides of 1.5 and 2.0, respectively. After 3000 cycles, MEA images were obtained by scanning electron microscopy (SEM).

## 5.3 Differences of mechanical degradation by GDL anisotropy during wet/dry cycles

To identify mechanical durability according to GDL anisotropy, wet/dry cycles were conducted. As indicator of fuel cell durability during the wet/dry cycles, I-V performance, HRF, and hydrogen crossover rate were measured. Also, surface morphology of MEA was obtained after 3000 cycles.

### 5.3.1 I-V performances

Fig. 5.3 shows the electrochemical I–V performance changes in the 90° and 0° GDL fuel cells at RH 100% conditions. Each fuel cell was clamped in different directions: i.e., 0° and 90° GDLs. As shown in Figs. 5.3 (a) and (b), the fuel cell performance was measured using the constant current method every 1000 cycles. After 3000 cycles, the cell potentials of the 90° GDL and 0° GDL fuel cell at 0.8 A/cm$^2$ decreased by 9.2 % and 15.6 %, respectively. At 1.2 A/cm$^2$, the cell potentials of the 90° GDL and 0° GDL fuel cells decreased by 12.9 % and 27.3 %, respectively. The supply of hydrogen/air to the anode and cathode can induce both chemical and mechanical degradations. However, when air/air is supplied to both the anode and cathode, the fuel cell performance decreases by mechanical degradation only. Thus, the performance decrease rate in this study was lower for even the 0° GDL fuel cell than in the previous study [40] when hydrogen/air was used at

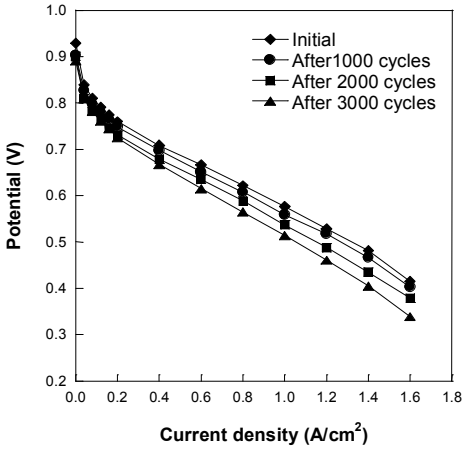


**(a) 90° GDL cell**

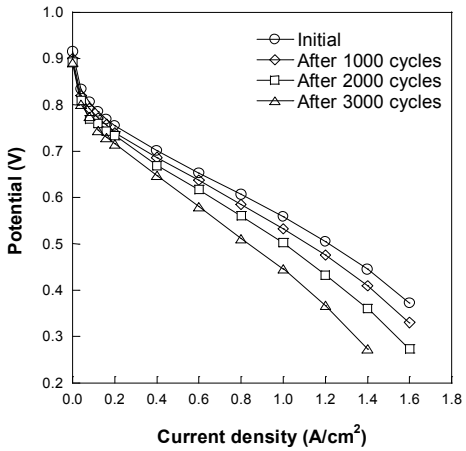


**(b) 0° GDL cell**

**Fig. 5. 3** Potential variations in fuel cells with different GDLs as a function of current density.

the anode and cathode. Fig. 5.4 shows the I–V performance of the 90° and 0° GDL fuel cells after 3000 wet/dry cycles. With a high current density, the potential decrease in the 90° GDL fuel cell was lower than that of the 0° GDL fuel cell, whereas the limiting current density was higher. Fig. 5.5 shows the potential variations in the fuel cells with 0° and 90° GDLs with an open circuit and other current densities of 0.6 and 1.2A/cm$^2$. The results confirmed that the potential in the 0° GDL fuel cell decreased more considerably than that in the 90° GDL fuel cell. The voltage variation in the 0° GDL fuel cell was higher than that in the 90° GDL fuel cell at a high current density. In particular, the performance difference between the 90° and 0° GDL cells appeared to be significant after 3000 cycles. For example, at the initial condition and after 3000 cycles, the voltage differences between the 90° GDL and 0° GDL cells were 0.020 and 0.094 V, respectively at 0.4 A/cm$^2$ and 1.2 A/cm$^2$. However, the voltage differences in the open circuit condition between the 90° GDL and 0° GDL cells appeared to be much smaller than that for other current densities.

### 5.3.2 HFR measurements

GDL intrusion into the gas channel and deformation decreased the cell

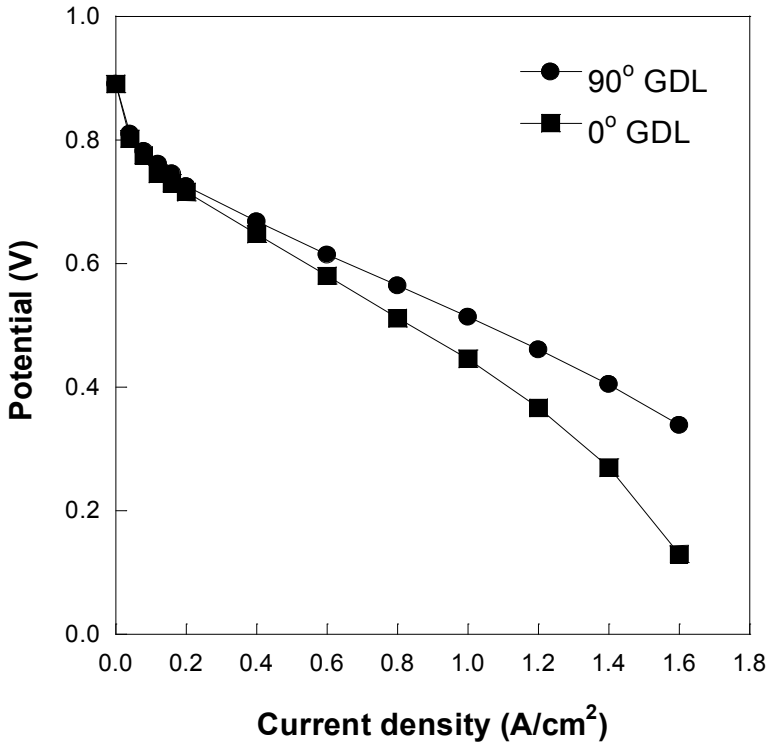


**Fig. 5. 4** I-V performance in fuel cells with different GDLs as a function of current density after 3000 wet/dry cycles.

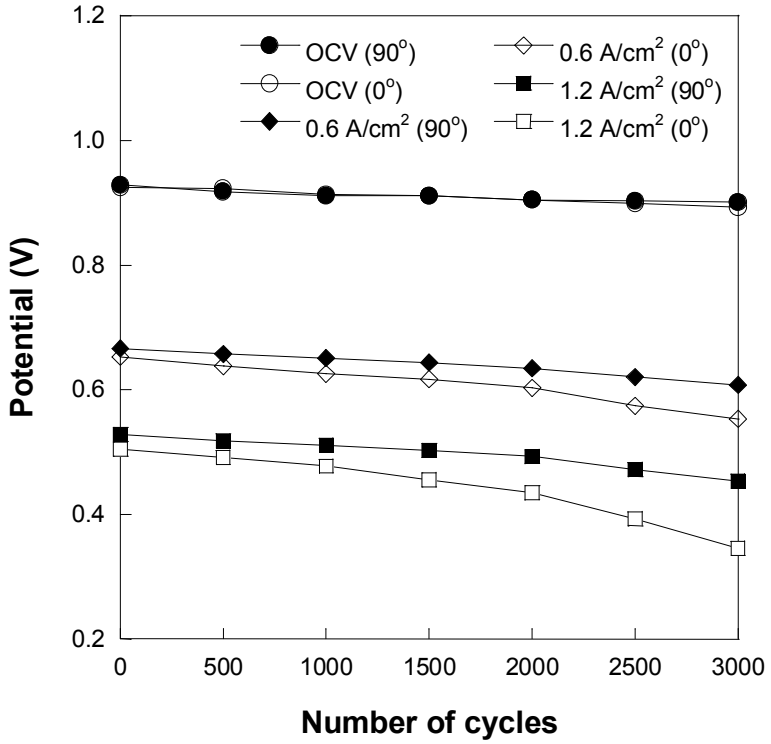


**Fig. 5. 5** Performance changes in fuel cells at OCV, 0.6 and 1.2 A/cm$^2$ every 500 wet/dry cycles.

performance and accelerated fuel cell degradation. In particular, the membrane swelled owing to water absorption as the RH increased. Membrane swelling compressed GDLs under the land, which then protruded into the channel; the local contact forces changed owing to redistribution of the stress field in the fuel cell [41-42]. In other words, the contact resistance between the MEA and GDL may change by swelling/shrinkage of the membrane during wet/dry cycles. For clarifying the effect of wet/dry cycles on contact resistance, the HFRs of the 0° and 90° GDLs fuel cells were measured. HFR has been often used to measure the electrical contact resistance associated with the interfaces between various fuel cell components. This study measured HFR every 500 cycles to investigate the effects of anisotropic GDLs (0/90°) on MEA degradation. Fig. 5.6 shows the HFR values of the fuel cells before and after wet/dry cycles at RH 100%. The HFR values of both cells significantly increased after 3000 wet/dry cycles and the HFR values of the 90° GDL fuel cell were lower than those of the 0° GDL fuel cells under all conditions. The difference in the HFR values between the 90° and 0° GDLs fuel cells clearly increased after 3000 cycles.

Figs. 5.7 (a) and (b) shows the HFR variations in the 90° and 0° GDL cells as a function of the number of cycles. The HFR values of the 90° GDL fuel cell were lower than those of the 0° GDL fuel cell under all conditions. Also,

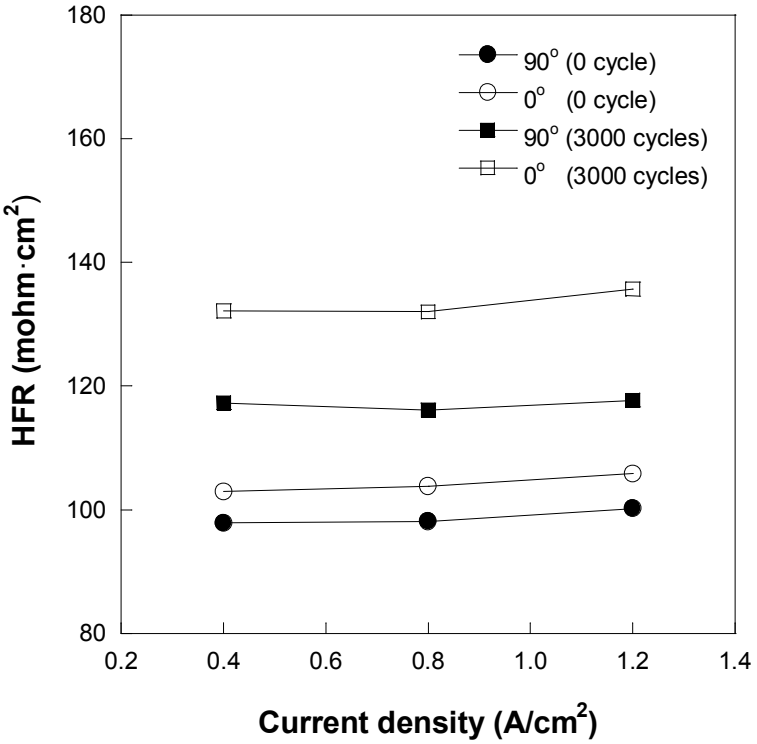


**Fig. 5. 6** High frequency resistances of 90° and 0° GDL cells before and after wet/dry cycles.

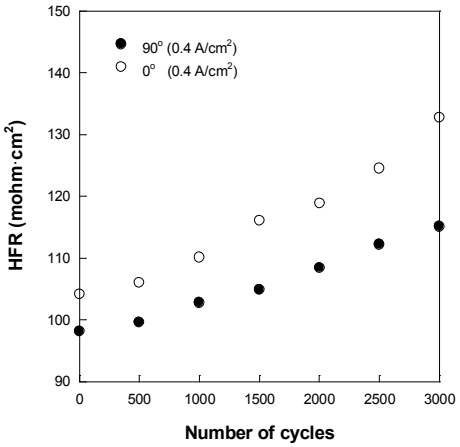


**(a) 0.4 A/cm$^2$**

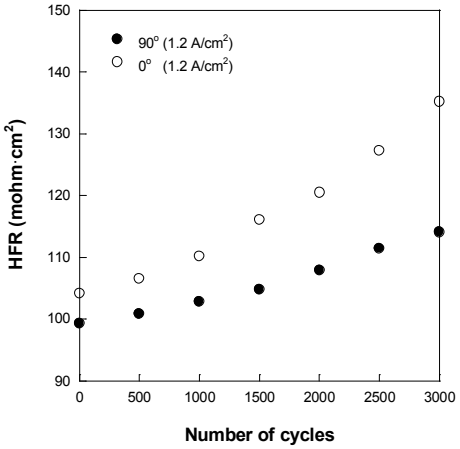


**(b) 1.2 A/cm$^2$**

**Fig. 5. 7** High frequency resistances of 90° and 0° GDL cells as a function of the cycle numbers.

the HFR values of the 90° GDL fuel cell increased slower than those of the 0° GDL fuel cell at both 0.4 (a) and 1.2 A/cm$^2$ (b) as the number of wet/dry cycles increased. The results indicate that the contact resistance of the 90° GDL fuel cell may be lower than that of the 0° GDL fuel cell because the former appears to be more resistant to intrusion into gas channel or deformation when the fuel cells are compressed. This higher resistance of the 90° GDL fuel cell may lead to more intimate contact at interfaces among the components of the 90° GDL fuel cell. Consequently, the 90° GDL fuel cell may have lower possibility of GDL deformation by repetitive swelling/shrinkage of the membrane during wet/dry cycles.

### 5.3.3 Hydrogen crossover rate through the membrane

Recently, thinner membranes have been widely adopted to reduce the electrical ohmic overvoltage and improve cell performance. However, these thinner membranes can increase the hydrogen crossover rate through the membrane and reduce fuel cell durability [43]. In our study, the hydrogen crossover rate was thus used as an indicator of mechanical degradation of the membrane by GDL anisotropy. A mass spectrometer was connected to the exit of the cathode channel to measure the hydrogen crossover rate. Fig. 5.8

shows hydrogen crossover rates after wet/dry cycles at RH 100% and a hydrogen pressure of 1.0 bar. The hydrogen crossover rates of both the 0° and 90° GDL fuel cells increased with the number of cycles. For instance, after 3000 cycles, the hydrogen concentration at the cathode channel outlet of the 90° and 0° GDL fuel cells increased from 357 and 351 ppm to 484 and 554 ppm, respectively. The 0° GDL fuel cell had a higher hydrogen crossover rate than the 90° GDL. However, the difference between hydrogen crossover rates of the 90° GDL and 0° GDL cells was quite smaller than our expectation of mechanical membrane failure such as pinholes, which can induce a much higher hydrogen crossover rate. Nevertheless, it is estimated that the differences of hydrogen crossover rates can be accelerated if the cell experiences longer cycles and membrane degradation is severe.

### 5.3.4 Morphology of MEA

To analyze the effects of the wet/dry cycles on the mechanical degradation of the MEA, the MEA morphology was obtained using SEM. Figs. 5.9 (a) shows the cathode catalyst layers (CLs) surface of a pristine MEA. Fig. 5.9 (b) and (c) shows the surface morphology of the cathode CLs of MEAs after 3000 wet/dry cycles with the land and channel regions

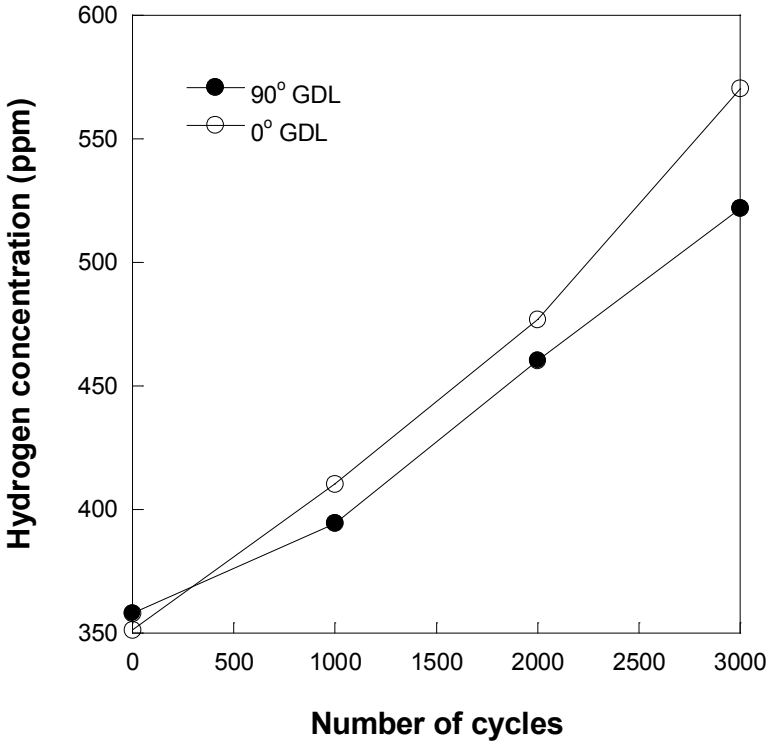


**Fig. 5. 8** Hydrogen crossover rates of 90° and 0° GDL cells at RH 100% as a function of the cycle numbers.

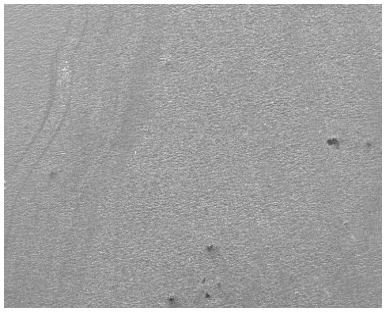

**(a) Pristine MEA**

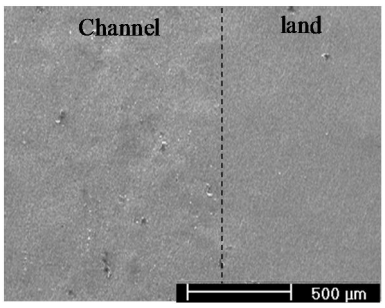


**(b) 90° GDL fuel cell after 3000 cycles**

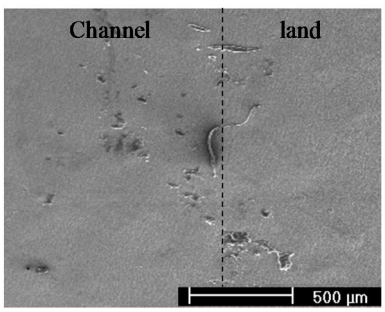


**(c) 0° GDL fuel cell after 3000 cycles**

**Fig. 5. 9** Surface morphology of MEA by observed by SEM.

represented by dotted lines. For the surface morphology, the specimens taken at same location of each MEA were obtained. The MEA surface morphology of 90° and 0° GDL fuel cell appeared to more degradation than the pristine MEA surface. Degradation of the MEA surfaces under the land was more severe than that under the channel because the MEA is mechanically pressed by bipolar plates during cell assembly. More noteworthy is that the degradation under channel of 0° GDL fuel cell was more severe than that of 0° GDL fuel cell. This result indicates that the membrane swelling/shrinkage by wet/dry cycles may induce deformation of the MEA in contact with the GDL and that the 90° GDL fuel cell, which is more resistant to membrane swelling mitigate MEA deformation.

Based on the above results, the 90° GDL appears to be more resistant to cell compression than the 0° GDL. The anisotropic characteristic of the GDL may also influence the contact between the MEA and GDL when the fuel cell is assembled. For visually analyzing the difference in deformations by the 90° and 0° GDLs when the fuel cell is assembled, the cross-sectional morphology of the GDLs upon compression was observed, as shown in Fig. 5.10. A mock-up with the same width of the channel and land as the bipolar plate used in this study was applied. Compression was applied at 1.0 and 2.0 MPa. Although a spatial gap was not detected between the MEA and 90°

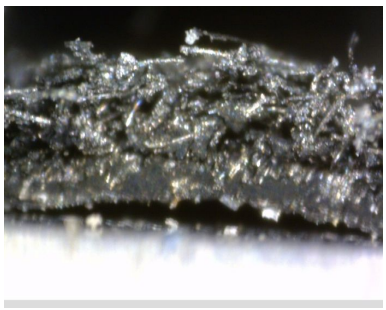

**(a) 0° GDL at 1.0 MPa**

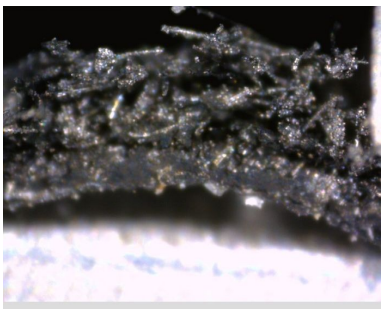

**(b) 0° GDL at 2.0 MPa**

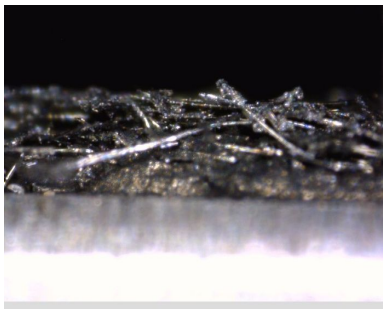

**(c) 90° GDL at 1.0 MPa**

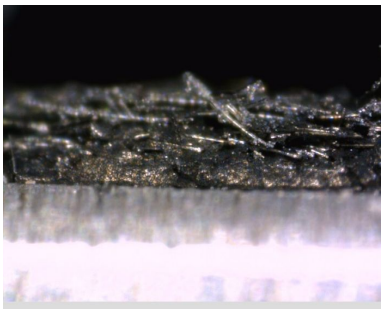

**(d) 90° GDL at 2.0 MPa**

**Fig. 5.10** Cross-sectional morphology upon compression: (a) 0° GDL / 1.0 MPa; (b) 0° GDL / 2.0 MPa; (c) 90° GDL / 1.0 MPa; (d) 90° GDL / 2.0 MPa.

GDL, one between the MEA and 0° GDL was detected, and the gap was bigger at higher compression. In other words, the deformation was more severe at a higher compression pressure for the 0° GDL, whereas there was almost no deformation observed for the 90° GDL. This confirmed the higher resistance of 90° GDL to cell assembly compression. The results indicate that the 0° GDL is subjected to more mechanical stress than the 90° GDL under the membrane swelling condition. As noted earlier, the membrane swells and shrinks when wet/dry gas is supplied into the fuel cell. This repetitive membrane swelling/shrinkage causes contact between the MEA and GDL to gradually become weaker, as shown in Fig. 5.11. Owing to this weaker contact, the rate of GDL deformation increase, and thus the increase in contact resistance is accelerated. Therefore, the 90° GDL cell may less prone to deformation owing to greater contact stability between the MEA and GDL. Thus, mechanical degradation of the 90° GDL cell by wet/dry cycles can be mitigated relative to the 0° GDL cell.

## 5.4 Summary

In this chapter, the effect of in-plane anisotropic characteristics on the mechanical degradation of an MEA was investigated using an AST. The

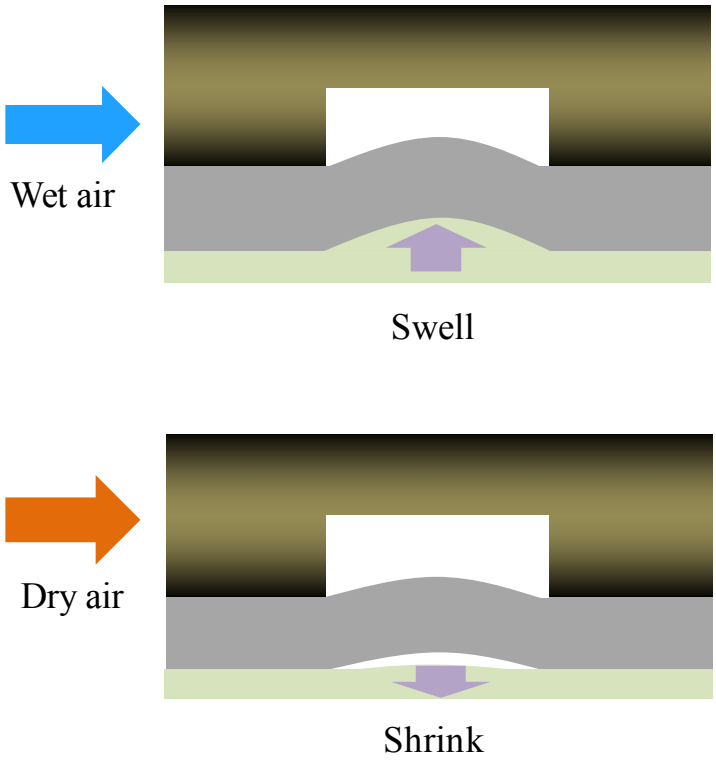


**Fig. 5.11** Schematic diagram of membrane swelling/shrinkage process for wet/dry cycles.

wet/dry cycling method was adopted to cause mechanical degradation of the MEA. Before the start of wet/dry cycles, the initial I–V performances, HFRs, and hydrogen crossover rates were measured. The I–V performances and HFRs of the 90° GDL fuel cell, whose higher bending stiffness direction is perpendicular to the direction of the major flow field, and 0° GDL fuel cell, whose higher bending stiffness direction is parallel to the direction of the major flow field, were measured every 500 cycles and hydrogen crossover rates were measured every 1000 cycles. I–V performance and HRF drop of the 0° GDL fuel cell according to wet/dry cycles was higher because the 0° GDL had lower resistance to stress by repetitive membrane swelling/shrinkage than the 90° GDL. The increase in the hydrogen crossover rate of the 0° GDL fuel cell was higher than that of the 90° GDL fuel cell because of mechanical degradation of the MEA. Through SEM, it was shown that the MEA deformation of 0° GDL fuel cells was more severe than that of the 90° GDL fuel cell after 3000 cycles. No spatial gap due to deformation of the 90° GDL under compression was detected; however, a gap for the 0° GDL was observed. These results support our assumptions that a higher resistance of the GDL to repetitive membrane swelling/shrinkage by wet/dry cycles increases the performance and durability of the fuel cell.

# Chapter 6. Concluding remarks

Deformation of components during fuel cell assembly is crucial factors to decrease cell performance and durability. In particular, deformation of GDL playing important roles including reactant gas transportation, electron conduction, liquid water management and structural supporting of MEA vitally influence on cell performance and durability. Accordingly, minimization of GDL deformation during cell assembly is very important. Commonly, GDL is composed with macro-porous layer and micro-porous layer. The macro-porous layer of the GDL has anisotropic characteristics by preferential direction of mechanical properties. The in-plane anisotropy of GDL has both fiber directions that is perpendicular (designated by 90° GDL) and parallel (designated by 0° GDL) to the major flow when fuel cell components are assembled. Deformation and intrusion into the cell channels of GDL are inevitable during the cell assembly. Mechanical bending stiffness direction by the in-plane anisotropy can influence on the GDL deformation/intrusion and accordingly, the cell performance and durability. For analyzing clearly the effects of the GDL in-plane anisotropy, experimental and numerical studies are conducted.

In the first part, the effects of GDL in-plane anisotropy on cell performance were investigated experimentally. For analyzing correlation

between anisotropic bending stiffness of a GDL and geometries of bipolar plates, 6 bipolar plates having 3 different channel/land width ratios and 3 different channel depths are prepared. I-V performance of the fuel cells with 90° GDL are generally higher than those with 90° GDL. On the contrary, high-frequency resistance (HFR) of the fuel cells with 90° GDL is lower than those with 0° GDL due to the higher resistance to force of bipolar plates during fuel cell assembly. In experimental results by different channel/land width ratios, the differences of I-V performances and HFR values between 90° and 0° GDL cells gradually decrease with increasing land/channel width ratio. It is because that anisotropic stiffness effect of the GDLs with wider land is reduced due to the better support. Therefore, less deformation and intrusion into channel of fuel cells with 90° GDL can improve the fuel cell performance. Air pressure drop of all the fuel cells with 90° GDLs was similar to those with 0° GDLs because air flow in channel at sufficient wide channel height of 0.6 mm. In experimental results by different channel depths, the differences of air pressure drop values between the 90° and 0° GDL cells were appeared. In shallowest channel, the air pressure drop values of the 0° GDL cells were clearly higher than those of the 90° GDL cells due to more intrusion of 0° GDL into the channel. However, other channels except the shallowest channel appear no significant difference presumably

due to the exceptional increase in the air pressure may cause more deformation and poor contact status of the GDLs in the fuel cell. These results are also supported the cross-sectional image showing the difference of blocked channel area between 0° and 90° GDL. Also, purge characteristics of fuel cell in dead-end mode were analyzed. The peak voltage of the 0° GDL cell was also higher than 90° GDL indicating the higher contact resistance in 0° GDL cell. Also, the purge interval of the fuel cell with 0° GDL was also longer than that of the fuel cell with 90° GDL implying the difference of GDL porosity reduction between both to 90° and 0° GDL cells at same cell assembly pressure. The averaged voltages of 90° GDL cell were higher than those of 0° GDL cell and the difference is more obvious at higher current density owing to the higher contact resistance in the higher current density.

In the next part, numerical model using commercial computational fluid dynamics (CFD) was conducted for analyzing the effect of anisotropic GDLs on cell performance by gas permeation through the cell channel. Permeability of anisotropic GDLs for applying to model simulation was measured. Afterwards, same geometry as single cell used in chapter 3 was applied in this model. The voltage difference in high current density over 0.9 $A/cm^2$ was relatively distinct, whereas the voltage difference in low current

density below 0.9 A/cm$^2$ was negligible. The simulation results show that the higher performance was induced by gas permeation through the cell channels. By the result, it is identified that not only contact resistance by GDL deformation but also gas permeation through the cell channel influence on the cell performance.

In the last part, the effect of in-plane anisotropic characteristics on the mechanical degradation of an MEA was investigated using an AST. The wet/dry cycling method was adopted to cause mechanical degradation of the MEA. I–V performances and HFRs of the 90° GDL cell and 0° GDL cell were measured every 500 cycles and hydrogen crossover rates were measured every 1000 cycles. I–V performance and HRF drop of the 0° GDL fuel cell according to wet/dry cycles was higher because the 0° GDL had lower resistance to stress by repetitive membrane swelling/shrinkage than the 90° GDL. The increase in the hydrogen crossover rate of the 0° GDL fuel cell was higher than that of the 90° GDL fuel cell because of mechanical degradation of the MEA. Through SEM, it was shown that the MEA deformation of 0° GDL fuel cells was more severe than that of the 90° GDL fuel cell after wet/dry cycles. No spatial gap due to deformation of the 90° GDL under compression was detected; however, a gap for the 0° GDL was observed. These results support our assumptions that a higher resistance of

the GDL to repetitive membrane swelling/shrinkage by wet/dry cycles increases the performance and durability of the fuel cell.

It was identified that cell performance can be improved by simple adjustment of GDL arrangement during cell assembly. The results about the effects by geometry of bipolar plates can be helpful for optimum designs of fuel cell components. Also, this effort to minimize the GDL deformation and degradation will bring forward the commercialization of PEMFC.

# References

[1] Ge J, Higier A, Liu H. Effect of gas diffusion layer compression on PEM fuel cell performance. Journal of Power Sources 2006;159:922-927.

[2] Zhou P, Wu CW, Ma GJ. Contact resistance prediction and structure optimization of bipolar plates. Journal of Power Sources 2006;159:1115-1122.

[3] Chi PH, Chan SH, Weng FB, Su A, Sui PC, Djilali N. On the effects of non-uniform property distribution due to compression in the gas diffusion layer of a PEMFC. International Journal of Hydrogen Energy 2010;35:2936-2948.

[4] Bapat CJ, Thynell ST. Effect of anisotropic thermal conductivity of the GDL and current collectro rib width on two-phase transport in a PEM fuel cell. Journal of Power Sources 2008;179:240-251.

[5] Pasaogullari U, Mukherjee, Wang CY, Chen KS. Anisotropic heat and water transport in a PEFC cathode gas diffusion layer. Journal of The Electrochemical Society 2007;154(8):B823-B834.

[6] Ju H. Investigation of the effects of the anisotropy of gas diffusion layers on heat and water transport in polymer electrolyte fuel cells. Journal of Power Sources 2009;191:259-268.

[7] Pfrang A, Veyret D, Sieker F, Tsotridis G. X-ray computed tomography of gas diffusion layers of PEM fuel cells: calculation of thermal conductivity. International Journal of Hydrogen Energy 2010;35:3751-3757.

[8] Fluckiger R, Freunberger SA, Kramer D, Wokaun A, Scherer GG, Anisotropic, effective diffusivity of porous gas diffusion layer materials for PEFC. Electrochim Acta 2008;54:551-559.

[9] Ahmed DH, Sung HJ, Bae J. Effect of GDL permeability on water and thermal management in PEMFCs – I. Isotropic and anisotropic permeability. International Journal of Hydrogen Energy 2008;33:3767-3785.

[10] Ahmed DH, Sung HJ, Bae J. Effect of GDL permeability on water and thermal management in PEMFCs - Ⅱ. Clamping force. International Journal of Hydrogen Energy 2008;33:3786-3800.

[11] Hao L, Cheng P. Lattice Boltzmann simulations of anisotropic permeabilityies in carbon paper gas diffusion layers. Journal of Power Sources 2009;186:104-114.

[12] Bapat CJ, Thynell ST. Effect of anisotropic electrical resistivity of gas diffusion layers (GDLs) on current density and temperature distribution in a polymer electrolyte membrane (PEM) fuel cell. Journal of Power

Sources 2008;185:428-432.

[13] Kleemann J, Finsterwalder F, Tillmetz W. Characterisation of mechanical behaviour and coupled electrical properties of polymer electrolyte membrane fuel cell gas diffusion layers. Journal of Power Sources 2009;190:92-102.

[14] Serincan MF, Pasaogullari U, Effect of gas diffusion layer anisotropy on mechanical stresses in a polymer electrolyte membrane. Journal of Power Sources 2011;196:1314-1320.

[15] Naing KSS, Tabe Y, Chikahisa T. Performance and liquid water distribution in PEFCs with different anisotropic fiber directions of the GDL. Journal of Power Sources 2011;196:2584-2594.

[16] Han K, Hong BK, Kim SH, Ahn BK, Lim TW. Influence of anisotropic bending stiffness of gas diffusion layers on the electrochemical performances of polymer electrolyte membrane fuel cells. International Journal of Hydrogen Energy 2010;35:12317-12328.

[17] Ph. Moçotéguy, Druart F, Bultel Y, Besse S, Rakotondrainibe A. Monodimensional modeling and experimental study of the dynamic behavior of proton exchange membrane fuel cell stack operating in dead-end mode. Journal of Power Sources 2007;167:349-357.

[18] Choi JW, Hwang YS, Seo JH, Lee DH, Cha SW, Kim MS. An

experimental study on the purge characteristics of the cathodic dead-end mode PEMFC for the submarine or aerospace applications and performance improvement with the pulsation effects. International Journal of Hydrogen Energy 2010;35:3698-3711.

[19] Choi JW, Hwang YS, Cha SW, Kim MS. Experimental study on enhancing the fuel efficiency of an anodic dead-end mode polymer electrolyte membrane fuel cell by oscillating the hydrogen. International Journal of Hydrogen Energy 2010;35:12469-12479.

[20] Sasmito AP, Mufumdar AS. Performance evaluation of a polymer electrolyte fuel cell with a dead-end anode: A computational fluid dynamic study. International Journal of Hydrogen Energy 2011;36:10917-10933.

[21] Ju H. Investigation of the effects of the anisotropy of gas-diffusion layers on heat and water transport in polymer electrolyte fuel cells. Journal of Power Sources 2009;191:259-268.

[22] Wu R, Zhu X, Liao Q, Wang H, Ding Y-d, Li J, et al. Determination of oxygen effective diffusivity in porous gas diffusion layer using a three-dimensional pore network model. Electrochem Acta 2010;55:7394-403.

[23] Yang WW, Zhao TS, He YL. Modelling of coupled electron and mass transport in anisotropic proton-exchange membrane fuel cell electrodes.

Journal of Power Sources 2008;185:765-775.

[24] He G, Yamazaki Y, Abudula A. A three-dimensional analysis of the effect of anisotropic gas diffusion layer(GDL) thermal conductivity on the heat transfer and two-phase behavior in a proton exchange membrane fuel cell(PEMFC). Journal of Power Sources 2010;195:1551-1560.

[25] N. L. Garland, T. G. Benjamin, J. P. Kopasz DOE fuel cell program: durability technical targets and testing protocols. ECS Transactions 2007;11:923-31.

[26] Merzouguia B, Swathirajan S, Rotating disk electrode investigations of fuel cell catalyst degradation due to potential cycling in acid electrolyte. Journal of Electrochem Society 2006; 153(12):A2220-6.

[27] Pierpont D, Hicks M, Watschke T, Turner P. Accelerated testing and lifetime modeling for the development of durable fuel cell MEAs. ECS Trans 2006;1(8):229-37.

[28] Kusoglu A, Karlsson AM, Santare MH, Cleghorn S, Johnson WB. Mechanical response of fuel cell membranes subjected to a hygro-thermal cycle. Journal of Power Sources 2006; 161(2) :987-96.

[29] Liu D, Case S. Durability study of proton exchange membrane fuel cells under dynamic testing conditions with cyclic current profile. Journal of Power Sources 2006;162(1):521-31.

[30] Liu W, Cleghorn S. Effects of relative humidity on membrane durability in PEM fuel cells. ECS Trans 2006;1(8): 263-73.

[31] Shengsheng Z, Xiaozi Y, Haijiang W, Walter M. Hong Z, Jun S. Shaohong W. Jiufun Z. A review of accelerated stress tests of MEA durability in PEM fuel cells. . International Journal of Hydrogen Energy 2009;33:388-404.

[32] Reiser CA, Bregoli L, Patterson TW, Yi JS, Yang JD, Perry ML, Jarvi TD. A reverse-current decay mechanism for fuel cells. Electrochemical and Solid-State Letters 2005;8:A273-276.

[33] Lee SY, Cho EA, Lee JW, Kim HJ, Lim TH, Oh IH, Won J. Effects of purging on the degradation of PEMFCs operating with repetitive on/off cycles. Journal of Electrochemical Society 2007;154:B194.

[34] Eom KS, Kim GH, Cho EA, Jang JH, Kim HJ, Yoo SJ, Kim SK, Hong BK. Effects of Pt loading in the anode on the durability of a membrane-electrode assembly for polymeer electrolyte membrane fuel cells during startup/shutdown cycling. International Journal of Hydrogen Energy 2009;33:388-404.

[35] McDonald RC, Mittelsteadt CK, Thompson EL. Effects of deep temperature cycling on Nafion 112 membranes and membrane electrode assemblies. Fuel Cells 2004;4(3): 208-213.

[36] Lim SJ, Park GG, Park JS, Sohn YJ, Yim SD, Yang TH, Hong BK, Kim CS. Investigation of freeze/thaw dureability in polymer elecyrolyte fuel cells. International Journal of Hydrogen Energy 2009;23:13111-13117.

[37] Zhang S, Yu H, Zhu H, Hou J, Yi B, Ming P. Effects of freeze/thaw cycles and gas purging method on polymer electrolyte membrane fuel cells. Chinese Journal of Chemical Engineering 2006;14(6):802-805.

[38] Huang X, Solasi R, Zou Y, Feshler M, Reifsnider K, Condit D, Burlatsky S, Madden T. Mechanical endurance of polymer electrolyte membrane and PEM fuel cell durability. Journal of Polymer Science Part B Polymer Physics 2066;44:2246-2257.

[39] Tang HL, Shen PK, Jiang SP, Wang F, Pan M. A degradation study of Nafion proton exchange membrane of PEM fuel cells. Journal of Power Sources 2007;170(1):85-92.

[40] Kang J, Kim J. Membrane electrode assembly degradation by dry/wet gas on a PEM fuel cell. International Journal of Hydrogen Energy 2010;35:13125-130.

[41] Zhou Y, Lin G, Shih AJ, Hu SJ. Assembly pressure and membrane swelling in PEM fuel cells. Journal of Power Sources 2009;192:544-551.

[42] Zhou Y, Lin G, Shih AJ, Hu SJ. Multiphysics modeling of assembly

pressure effects on proton exchange membrane fuel cell performance. ASME Journal of Fuel Cell Science and Technology 2009;6:041005-1-7.

[43] Baik KD, Hong BK, Kim MS. Effects of operating parameters on hydrogen crossover rate through Nafion membranes in polymer electrolyte membrane fuel cells. Renewable Energy 2013;57:234-239.

[44] W.-k. Lee, C.-H. Ho, J.W. Van Zee, M. Murthy, The effects of compression and gas diffusion layers on the performance of a PEM fuel cell, Journal of Power Sources 1999; 45-51.

[45] Jiabin G, Andrew H, Hongtan Liu. Effect of gas diffusion layer compression on PEM fuel cell performance. Journal of Power Sources 2009;159:922-927.

[46] Wen CY, Lin YS, Lu CH. Experimental study of clamping effects on the performances of a single proton exchange membrane fuel cell and a 10-cell stack. Journal of Power Sources 2009;192:475-485.

[47] Bladimir R-A, Joshua D. S, Abel H-G, Michael W. E. Experimental characterization of the water transport properties of PEM fuel cells diffusion media Journal of Power Sources 2012;218:221-232.

[48] Vlamir G, Michael J. B, Emory S. D, Yu-Min T, Thomas A, Zawodzinski J. Adin Mann J. Characterization of transport properties in gas diffusion layers for proton exchanbe membrane fuel cells 2. Absolute

permeability. Journal of Power Sources 2012;165:793-802.

[49] Hussaini IS, Wang CY. Measurement of relative permeability of fuel cell diffusion media. Journal of Power Sources 2012;195:3830-3840.

[50] Xing XQ, Lum KW, Poh HJ, Wu YL. Optimization of assembly clamping pressure on performance of proton-exchange membrane fuel cells. Journal of Power Sources 2010;195:62-68.

[51] Weng FB, Su A, LinYT, Jung GB, Chen YM. Novel testing method for fuel cell hardware design and assembly. Journal of Fuel Cell Science and Technology 2005;2:197-201.

[52] Chi PH, Chan SH, Weng FB, Su A, Sui PC, Djilali N. On the effects of non-uniform property distribution due to compression in the gas diffusion layer of a PEMFC. International Journal of Hydrogen Energy 2010;35:2936-2948.

[53] F.A.L. Dullien, Porous Media: Fluid Transport and Pore Structure, Academic Press, New York. 1992.

[54] Williams MV, Begg E, Bonville L, Kunz HR. Fenton JM. Characterization of gas diffusion layers for PEMFC, Journal of Electrochemcal Society. 151 (2004) 1173-1180.

[55] Ihonen J, Mikkola M, Lindbergh G. Flooding of gas diffusion backing in PEFCs: physical and electrochemcal characteriztion. Journal of

Electrochemical Society. 151 (2004) 1152-1161.

[56] Gostick JT, Fowler MW, Pritzker MD, Ioannidis MA, Behra LM. In-plane and through-plane gas permeability of carbon fiber electrode backing layers. Journal of Power Sources 2006;162:228-238.

[57] Geertsma J. Estimating the coefficient of inertial resistance in fluid flow through porous media. Journal of Petroleum Science and Engineering. 10 (1974) 445-450.

[58] ES-PEMFC methodology and tutorial manual, http://www.adapco.com.

[59] Shimpalee S, Greenway S, Van Zee J, The impact of channel path length on PEMFC flow-field design. Journal of Power Source 2004;135:79-87.

# 국 문 초 록

고분자 전해질 막 연료전지에서 가스확산층은 촉매층으로의 반응가스 이송, 전자의 전도, 촉매층에서 생성된 포화액의 원활한 배출, 그리고 연료전지 구성품의 체결시 기계적으로 막전극 접합체를 기계적으로 지지해주는 역할을 한다. 가스확산층을 제작할 때에 그 특성상 기계적 평면이방성을 가진다. 본 연구에서는 연료전지 주 유로에 평행하게 배치하여 조립되는 경우를 0도, 반대로 수직하게 배치하여 조립되는 경우를 90도 가스확산층으로 각각 정하였다. 연료전지가 조립될 때 가스확산층의 변형 혹은 유로측으로의 투과는 일어날 수 밖에 없는 현상으로 이러한 변형 및 투과성을 최소화 하는 것이 연료전지 성능을 향상시키는 중요한 요인이 된다. 따라서, 가스확산층의 평면 이방성에 따른 기계적 강성의 차이가 연료전지 체결시에 발생하는 변형 및 투과에 미치는 영향을 분석하고 최종적으로 성능 및 내구성에 미치는 영향을 실험 및 모델을 통해 분석하였다. 먼저 가스 확산층의 평면이방성에 따른 연료전지 성능 및 분리판의 기하구조에 따른 경향을 분석하기 위하여 유로의 채널부와 랜드부의 비에 따라서, 그리고 채널부의 깊이에 따라 각각 3개씩의 분리판을 제작하였다. 90도 가스확산층을 사용하는 연료전지가 0도 가스확산층을 사용하는 경우보다 모든 조건에서 성능이 높게 나왔으며 이는 연료전지 체결시 90도 가스확산층의 높은 기계적 강도에 따른 것으로 분석되었다. 또한, 분리판의 채널/랜드부의 비가 감소할수록 90도와 0도를 사용하는 연료전지의 성

능과 고주파저항의 차가 더 크게 나타났으며 이는 랜드부의 비가 감소할수록 가스확산층이 변형 및 침투되는 경향이 강하게 나타나기 때문으로 분석된다. 그리고 유로의 깊이의 증가에 따라서는 공기의 압력저하가 유로 깊이의 증가로 인하여 감소하므로 전반적으로 성능이 증가하였다. 다음으로 연료전지 유로의 랜드부 아래 가스확산층의 반응가스의 투과성이 성능에 미치는 영향을 분석하기 위한 해석을 수행하였다. 가스확산층의 이방성을 모사하기 위하여 가스 투과도를 측정하는 장치를 제작하여 90도와 0도의 가스 투과도를 측정하였다. 그 결과 90도 가스확산층의 투과도가 0도의 경우보다 높게 나왔으며 측정된 값은 모델에 적용하였다. 모델을 수행한 결과, 90도 가스확산층의 경우 유로의 랜드부 아래에서 보다 높은 투과가 발생하였으며 고전류밀도에서 더욱 그 차이가 높게 나타났다. 마지막으로 고분자 전해질 막의 반복적인 팽창과 수축으로 인한 막전극 접합체 및 가스확산층의 내구성에 미치는 영향을 분석하기 위하여 습/건조 공기를 반복적으로 주입하는 가속화 실험을 수행하였다. 3000회 반복 실험 결과 0도 가스확산층을 사용한 연료전지의 성능이 90도 가스확산층을 사용한 경우에 비해 성능 감소가 더욱확연히 나타났다. 또한 고주파 저항 및 크로스오버에서도 0도 가스확산층의 경우 그 증가율이 높게 나타났다. 이는 주사형 전자현미경을 사용하여 촬영된 이미지를 통해 검증되었다. 이러한 분석결과는 가스확산층의 평면이방성의 적용 및 분리판의 최적설계를 통하여 성능을 보다 향상 시킬 수 있을 뿐만 아니라, 내구성의 향상을 통하여 연료전지 시스템의 상용화를 앞당기기 위한 핵심 자료로써 활용 될 수 있을 것으로 기대한다.

주요어: 고분자 전해질막 연료전지, 가스확산층, 평면 이방성, 열화,
습/건조 가스 주입 사이클
학 번: 2010-30789